LETTER

Hepatocytes direct the formation of a pro-metastatic niche in the liver

Jae W. Lee[1,2], Meredith L. Stone[1,2], Paige M. Porrett[3], Stacy K. Thomas[1,2], Chad A. Komar[1,2], Joey H. Li[1,2], Devora Delman[1,2], Kathleen Graham[1,2], Whitney L. Gladney[1,2], Xia Hua[1,2], Taylor A. Black[1,2], Austin L. Chien[1,2], Krishna S. Majmundar[1,2], Jeffrey C. Thompson[1,2], Stephanie S. Yee[1,2], Mark H. O'Hara[1,2], Charu Aggarwal[1,2], Dong Xin[3], Abraham Shaked[3], Mingming Gao[4], Dexi Liu[4], Mitesh J. Borad[5], Ramesh K. Ramanathan[5,10], Erica L. Carpenter[1,2], Ailing Ji[6,7], Maria C. de Beer[7,8], Frederick C. de Beer[6,7], Nancy R. Webb[7,9] & Gregory L. Beatty[1,2]*

The liver is the most common site of metastatic disease[1]. Although this metastatic tropism may reflect the mechanical trapping of circulating tumour cells, liver metastasis is also dependent, at least in part, on the formation of a 'pro-metastatic' niche that supports the spread of tumour cells to the liver[2,3]. The mechanisms that direct the formation of this niche are poorly understood. Here we show that hepatocytes coordinate myeloid cell accumulation and fibrosis within the liver and, in doing so, increase the susceptibility of the liver to metastatic seeding and outgrowth. During early pancreatic tumorigenesis in mice, hepatocytes show activation of signal transducer and activator of transcription 3 (STAT3) signalling and increased production of serum amyloid A1 and A2 (referred to collectively as SAA). Overexpression of SAA by hepatocytes also occurs in patients with pancreatic and colorectal cancers that have metastasized to the liver, and many patients with locally advanced and metastatic disease show increases in circulating SAA. Activation of STAT3 in hepatocytes and the subsequent production of SAA depend on the release of interleukin 6 (IL-6) into the circulation by non-malignant cells. Genetic ablation or blockade of components of IL-6–STAT3–SAA signalling prevents the establishment of a pro-metastatic niche and inhibits liver metastasis. Our data identify an intercellular network underpinned by hepatocytes that forms the basis of a pro-metastatic niche in the liver, and identify new therapeutic targets.

To understand the mechanisms that underlie the formation of a pro-metastatic niche in the liver, we used the *LSL-Kras*[G12D/+]; *LSL-Trp53*[R172H/+];*Pdx1-cre* (KPC) mouse model of pancreatic ductal adenocarcinoma (PDAC)[4,5]. We looked for features of a pro-metastatic niche in the livers of over-16-week-old tumour-bearing KPC mice and 8- to 10-week-old non-tumour-bearing (NTB) KPC control mice, which lack PDAC but harbour pancreatic intraepithelial neoplasia (PanIN)[6]. Compared to control mice, the livers of KPC mice contained increased numbers of myeloid cells, accompanied by an increase in the deposition and expression of fibronectin and type I collagen (COL1) (Fig. 1a, Extended Data Fig. 1a–d). Orthotopic implantation of KPC-derived PDAC cells into wild-type mice recapitulated these changes (Extended Data Fig. 1e–i). As shown previously[7,8], matrix deposition did not require myeloid cells (Extended Data Fig. 1j–l). These results are consistent with evidence that myeloid cell accumulation and extracellular matrix deposition are key components of a pro-metastatic niche[7–10].

We next evaluated the susceptibility of the liver to metastatic colonization. Yellow fluorescent protein (YFP)-labelled KPC-derived PDAC cells (PDAC–YFP)[6] were injected into control mice and KPC
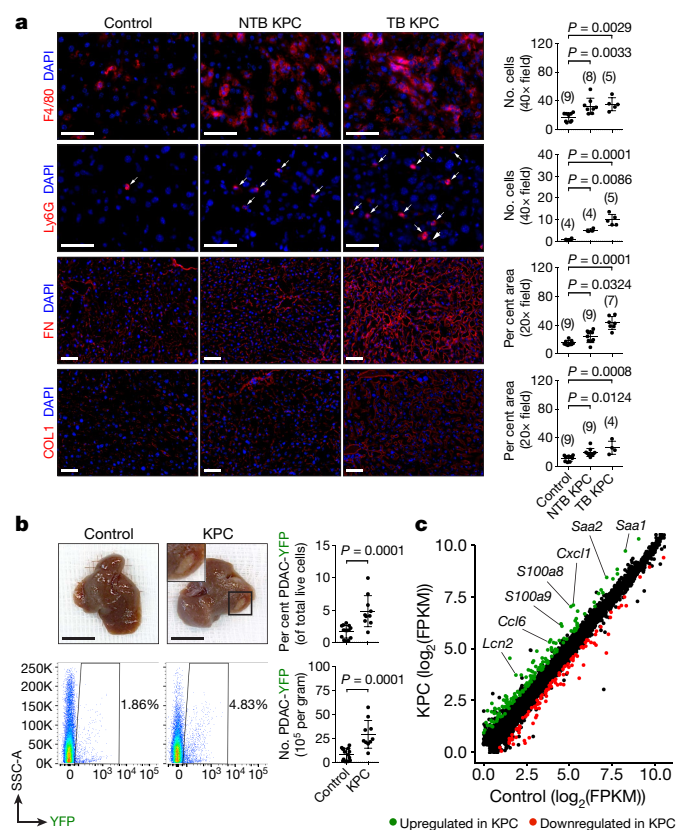

Fig. 1 | Primary PDAC development induces a pro-metastatic niche in the liver. a, Images and quantification of myeloid cells, fibronectin (FN), and COL1 in the liver. Arrows indicate Ly6G^{+} cells. Numbers in parentheses on plots indicate the number (n) of mice. Data pooled from two experiments. TB, tumour-bearing; NTB, non-tumour-bearing. **b**, Images of the liver and quantification of PDAC–YFP cells. Control mice ($n = 14$) and NTB KPC mice ($n = 10$) were intrasplenically injected with PDAC–YFP cells, and the liver was analysed after 10 days. Data representative of two independent experiments. **c**, Scatter plot of transcriptome data. FPKM, fragments per kilobase of exon per million mapped fragments ($n = 5$ for both groups). Scale bars, 50 μm (**a**) and 1 cm (**b**). Statistical significance calculated using one-way analysis of variance (ANOVA) with Dunnett's test (**a**) and two-tailed Mann–Whitney test (**b**). Data represented as mean ± s.d.

[1]Abramson Cancer Center, University of Pennsylvania, Philadelphia, PA, USA. [2]Division of Hematology-Oncology, Department of Medicine, Perelman School of Medicine, University of Pennsylvania, Philadelphia, PA, USA. [3]Division of Transplant Surgery, Department of Surgery, Perelman School of Medicine, University of Pennsylvania, Philadelphia, PA, USA. [4]Department of Pharmaceutical and Biomedical Sciences, College of Pharmacy, University of Georgia, Athens, GA, USA. [5]Mayo Clinic Cancer Center, Mayo Clinic, Phoenix, AZ, USA. [6]Department of Internal Medicine, University of Kentucky, Lexington, KY, USA. [7]Saha Cardiovascular Research Center, University of Kentucky, Lexington, KY, USA. [8]Department of Physiology, University of Kentucky, Lexington, KY, USA. [9]Department of Pharmacology and Nutritional Sciences, University of Kentucky, Lexington, KY, USA. [10]Present address: Merck Research Labs, Rahway, NJ, USA. *e-mail: gregory.beatty@uphs.upenn.edu
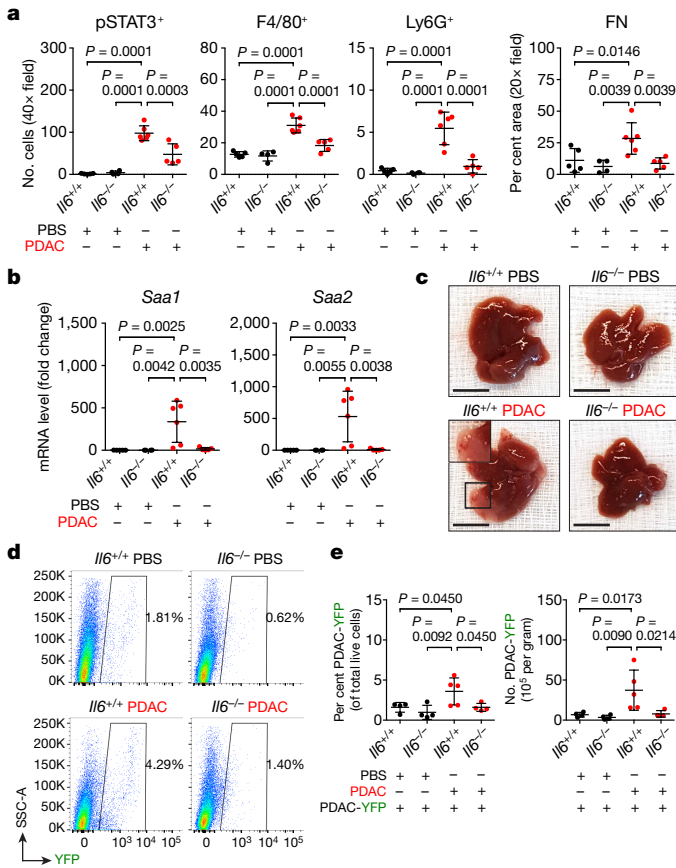
Fig. 2 | IL-6 is necessary for the establishment of a pro-metastatic niche in the liver. a, b, $n = 5$ and 6 for $Il6^{+/+}$ mice and $n = 4$ and 5 for $Il6^{-/-}$ mice orthotopically injected with PBS or PDAC cells, respectively. **a,** Quantification of pSTAT3$^+$ cells, myeloid cells, and fibronectin. **b,** mRNA levels of *Saa1* and *Saa2* in the liver. **c–e,** $n = 4$ and 5 for $Il6^{+/+}$ mice and $n = 4$ for $Il6^{-/-}$ mice orthotopically injected with PBS or PDAC cells, respectively. All groups were intraportally injected with PDAC–YFP cells on day 10. **c, d,** Images of liver and flow cytometric analysis. **e,** Quantification of PDAC–YFP cells. Data representative of two independent experiments (**a–e**). Scale bars, 1 cm. Statistical significance calculated using one-way ANOVA with Dunnett's test. Data represented as mean ± s.d.

Fig. 3 | STAT3 signalling in hepatocytes orchestrates the formation of a pro-metastatic niche in the liver. a, Study design for **b–f** ($n = 4$ for $Stat3^{flox/flox}$ mice injected with PBS or PDAC cells; $n = 8$ and 7 for $Stat3^{flox/flox}$ *Alb-cre* mice injected with PBS and PDAC cells, respectively). **b, c,** Quantification of pSTAT3$^+$ cells, myeloid cells, and fibronectin. **d,** mRNA levels of *Saa1* and *Saa2* in the liver. **e,** Images of *Saa1* and *Saa2* mRNA in liver cells. Dashed lines and asterisks indicate sinusoids and hepatocytes, respectively. **f,** Concentration of circulating SAA. Data representative of two independent experiments (**a–f**). Scale bars, 50 μm. Statistical significance calculated using one-way ANOVA with Dunnett's test. Data represented as mean ± s.d.

mice. The metastatic burden was threefold higher in KPC mice, and metastatic lesions were detected in the livers of KPC mice at increased frequency and size with enhanced proliferation (shown using Ki-67) (Fig. 1b, Extended Data Fig. 2a, b). Similar findings were observed using a YFP-negative KPC-derived cell line (Extended Data Fig. 2c, d). Orthotopic implantation of PDAC cells also increased the susceptibility of the liver to metastatic colonization, and this finding was independent of the presence of CD4$^+$ and CD8$^+$ T cells (Extended Data Fig. 2e–s).

We next performed mRNA sequencing on RNA isolated from the livers of control and KPC mice. We identified 275 differentially expressed genes (Extended Data Fig. 3a, b, Supplementary Data 1) and found that genes upregulated in KPC mice were associated with immune-related processes (Extended Data Fig. 3c). Notably, genes encoding myeloid chemoattractants, including SAA and members of the S100 family, were upregulated in KPC mice[11–13] (Fig. 1c, Extended Data Fig. 3d, e). We also found enrichment of immune-related pathways, particularly the IL-6–JAK–STAT3 signalling pathway (Extended Data Fig. 3f, Supplementary Table 1). We validated our results by examining the livers of KPC mice for the presence of phosphorylated STAT3 (pSTAT3). STAT3 was activated in 80–90% of hepatocytes from KPC mice, compared to less than 2% of hepatocytes in control mice (Extended Data Fig. 3g, h). By contrast, we did not detect activation
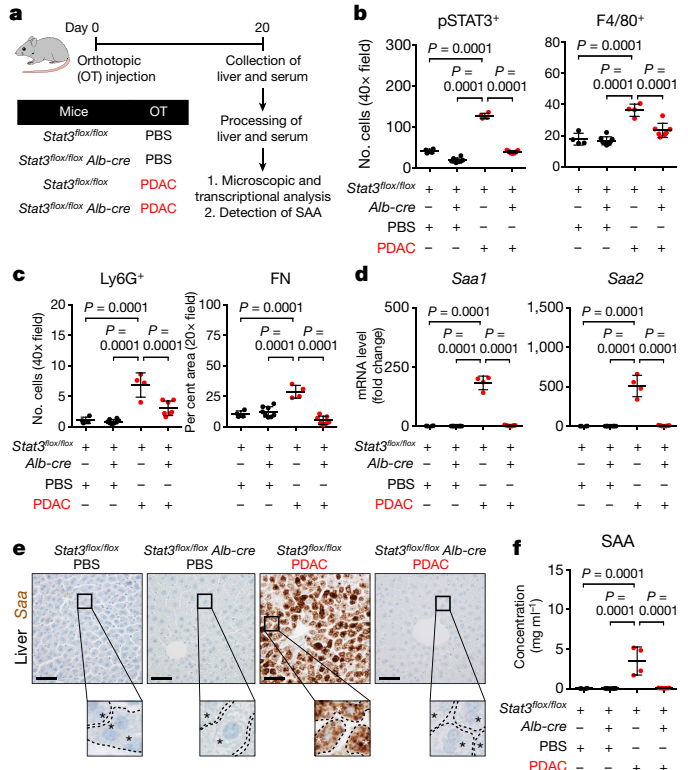
of STAT1 signalling (Extended Data Fig. 3i). Orthotopic implantation of PDAC cells also induced phosphorylation of STAT3 in hepatocytes (Extended Data Fig. 3j, k).

As IL-6 is fundamental to STAT3 signalling in hepatocytes[14], we examined the livers of control mice ($Il6^{+/+}$) and IL-6 knockout mice ($Il6^{-/-}$) orthotopically injected with PBS or PDAC cells. Tumour-implanted $Il6^{-/-}$ mice displayed a decrease in STAT3 activation, particularly in hepatocytes (Fig. 2a, Extended Data Fig. 4a). This loss in STAT3 activation was accompanied by reductions in myeloid cell accumulation and extracellular matrix deposition without alterations in the morphology and density of liver sinusoids (Fig. 2a and Extended Data Fig. 4a-d). We also observed reduced expression of SAA, other chemoattractants, and extracellular matrix proteins (Fig. 2b, Extended Data Fig. 4e). Genetic ablation of *Il6*, however, did not alter proliferation, vascular density, or primary tumour growth (Extended Data Fig. 4f, g). $Il6^{-/-}$ mice were also less susceptible than control mice to metastatic colonization, and blockade of the IL-6 receptor (IL-6R) similarly inhibited the formation of a pro-metastatic niche in the liver (Fig. 2c–e, Extended Data Fig. 4h–s). Notably, genetic ablation of *Il6* or blockade of IL-6R did not completely inhibit STAT3 signalling, suggesting that IL-6-independent mechanisms may contribute to STAT3 activation.

IL-6 promotes the development and progression of PDAC[15–18]. To identify the source of IL-6, we orthotopically injected PBS or PDAC cells into $Il6^{+/+}$ and $Il6^{-/-}$ mice and measured the concentration of IL-6 at distinct anatomic sites (Extended Data Fig. 5a). We detected IL-6 only in tumour-implanted $Il6^{+/+}$ mice, with the highest concentration
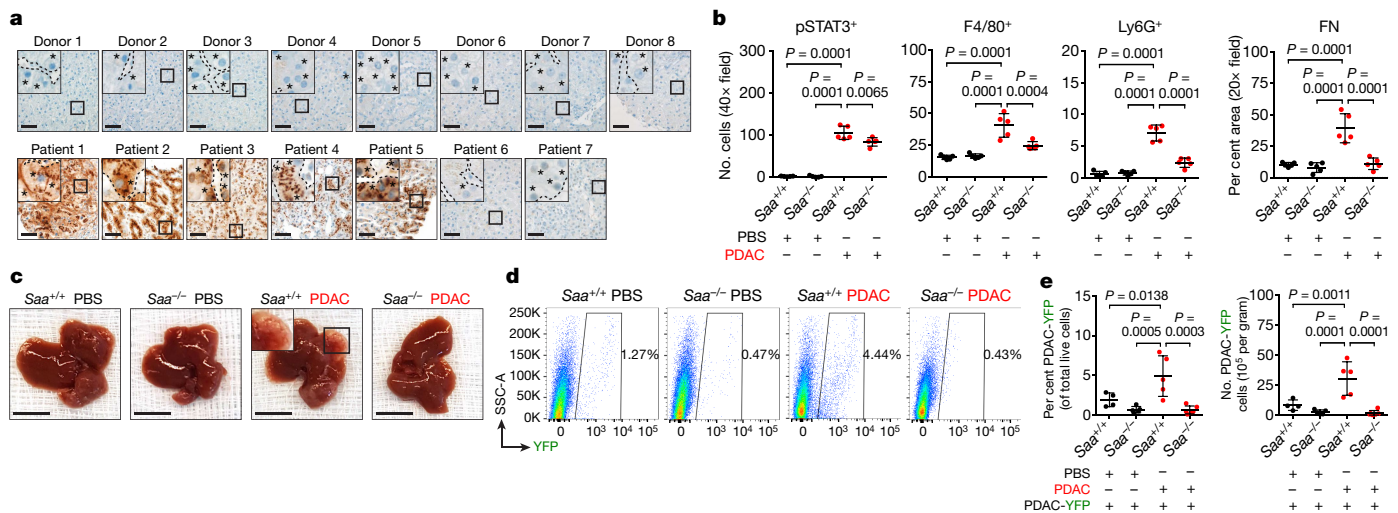
Fig. 4 | SAA is a critical determinant of liver metastasis. a, Images of SAA in the livers of healthy donors (top) and patients with PDAC with liver metastases (bottom). Dashed lines and asterisks indicate sinusoids and hepatocytes, respectively. Data representative of one experiment. **b**, Quantification of pSTAT3$^+$ cells, myeloid cells, and fibronectin ($n = 5$ for all groups orthotopically injected with PBS or PDAC cells). For **c–e**, $n = 4$ and 5 for $Saa^{+/+}$ mice and $n = 5$ and 6 for $Saa^{-/-}$ mice

orthotopically injected with PBS and PDAC cells, respectively. All groups were intraportally injected with PDAC–YFP cells on day 10. **c, d**, Images of liver and flow cytometric analysis. **e**, Quantification of PDAC–YFP cells. Data representative of two independent experiments (**b–e**). Scale bars, 50 μm (**a**) and 1 cm (**c**). Statistical significance calculated using one-way ANOVA with Dunnett's test. Data represented as mean ± s.d.

of IL-6 found in the primary tumour (Extended Data Fig. 5b, c). Although *Il6* mRNA was undetectable in the liver, lung, and malignant cells, we observed *Il6* mRNA in host cells adjacent to CK19-expressing PDAC cells (Extended Data Fig. 5d–g). Human primary tumours displayed a similar expression pattern (Extended Data Fig. 5h). Moreover, *Il6* mRNA was detected in α-SMA$^+$ stromal cells located adjacent to PanIN and PDAC cells in KPC mice (Extended Data Fig. 5i–k). We also found that primary pancreatic tumour supernatant activated STAT3 signalling in hepatocytes, and this was reduced in the presence of anti-IL-6R antibodies (Extended Data Fig. 6a, b). These results show that IL-6 released by non-malignant cells within the primary tumour is a key mediator of STAT3 signalling in hepatocytes.

To study a role for hepatocytes in directing liver metastasis, we generated mice that lacked *Stat3* in hepatocytes (*Stat3^{flox/flox} Alb-cre*). Compared to control mice (*Stat3^{flox/flox}*), tumour-implanted *Stat3^{flox/flox} Alb-cre* mice lacked features of a pro-metastatic niche (Fig. 3a–c, Extended Data Fig. 6c) and failed to produce SAA (Fig. 3d–f). However, deletion of *Stat3* in hepatocytes did not affect liver sinusoid density or morphology and did not alter the size, proliferation, or vascular density of the primary tumour (Extended Data Fig. 6d–f). The livers of tumour-implanted *Stat3^{flox/flox} Alb-cre* mice were also less susceptible to metastatic colonization (Extended Data Fig. 6g–l). In addition to its expression in hepatocytes (Extended Data Fig. 6m), mRNA for SAA was detected in colonic cells[19] and in cells present in the periphery of the primary tumour (Extended Data Fig. 6n). However, both cell types maintained comparable levels of SAA mRNA despite deletion of *Stat3* in hepatocytes.

SAA proteins are acute phase reactants[20]. Consistent with elevated levels of circulating SAA in tumour-implanted mice (Fig. 3f), patients with PDAC displayed elevated levels of circulating SAA (Extended Data Fig. 7a). Overexpression of SAA and pSTAT3 by hepatocytes was also observed in five of seven patients with liver metastases (Fig. 4a, Extended Data Fig. 7b). Notably, high levels of circulating SAA correlated with worse outcomes (Extended Data Fig. 7c). Elevated levels of circulating SAA were also observed in patients with non-small-cell lung carcinoma (NSCLC) with liver metastases, and overexpression of SAA by hepatocytes was detected in the livers of patients with colorectal carcinoma (CRC) (Extended Data Fig. 7d, e). In addition, compared to tumour-implanted control mice (*Saa^{+/+}*), double-knockout *Saa1^{-/-} Saa2^{-/-}* mice (hereafter referred to as *Saa^{-/-}* mice) implanted with PDAC or MC-38 CRC cells failed to show features of a pro-metastatic

niche in the liver, though genetic ablation of *Saa1* and *Saa2* had no effect on primary tumour growth (Fig. 4b–e, Extended Data Fig. 7f–s). SAA was also necessary for IL-6-mediated formation of a pro-metastatic niche and for fibrosis and myeloid cell recruitment in the setting of liver injury (Extended Data Fig. 8).

Tissue inhibitor of metalloproteinases 1 (TIMP1)[7,8] and macrophage migration inhibitory factor (MIF)[9,10] have been implicated in the promotion of metastasis. However, expression of these molecules was not affected by IL-6–STAT3–SAA signalling (Extended Data Fig. 9). We next determined whether formation of a pro-metastatic niche in the liver is dependent on the anatomical proximity of the pancreas to the liver. To this end, we looked for features of a pro-metastatic niche in the livers of CD45.1 and CD45.2 mice that were parabiotically joined (Extended Data Fig. 10a). Although only CD45.2 mice were implanted with PDAC cells, both mice displayed myeloid cell accumulation and fibrosis in the liver (Extended Data Fig. 10b–g), suggesting that formation of this niche is not dependent on the anatomical distance between the tumour and the liver. We also investigated whether SAA has a role in establishing a pro-metastatic niche in the lung. Development of PDAC in KPC mice induced accumulation of Ly6G$^+$ myeloid cells and deposition of fibronectin within the lung, but IL-6–STAT3–SAA signalling was not required for the formation of a pro-metastatic niche in the lung (Extended Data Fig. 10h–o).

Our data provide insight into the mechanisms that direct liver metastasis. Although recent studies have suggested a role for tumour-intrinsic factors in driving metastatic spread of cancer[7–10,21–23], we provide evidence that inflammatory responses mounted by hepatocytes are critical to liver metastasis. Mechanistically, hepatocytes orchestrate this process through activation of IL-6–STAT3 signalling and the subsequent production of SAA, which alters the immune and fibrotic microenvironment of the liver to establish a pro-metastatic niche (Extended Data Fig. 10p). Our findings suggest that therapies that target hepatocytes might prevent liver metastasis in patients with cancer.

Online content

Any methods, additional references, Nature Research reporting summaries, source data, statements of data availability and associated accession codes are available at https://doi.org/10.1038/s41586-019-1004-y.

1. Hidalgo, M. Pancreatic cancer. *N. Engl. J. Med.* **362**, 1605–1617 (2010).
2. Becker, A. et al. Extracellular vesicles in cancer: cell-to-cell mediators of metastasis. *Cancer Cell* **30**, 836–848 (2016).
3. Sceneay, J., Smyth, M. J. & Möller, A. The pre-metastatic niche: finding common ground. *Cancer Metastasis Rev.* **32**, 449–464 (2013).
4. Hingorani, S. R. et al. *Trp53R[172H]* and *KrasG12D* cooperate to promote chromosomal instability and widely metastatic pancreatic ductal adenocarcinoma in mice. *Cancer Cell* **7**, 469–483 (2005).
5. Lee, J. W., Komar, C. A., Bengsch, F., Graham, K. & Beatty, G. L. Genetically engineered mouse models of pancreatic cancer: the KPC model (*LSL-KrasG12D/+;LSL-Trp53R172H/+;Pdx-1-Cre*), its variants, and their application in immuno-oncology drug discovery. *Curr. Protoc. Pharmacol.* **73**, 14.39.1–14.39.20 (2016).
6. Rhim, A. D. et al. EMT and dissemination precede pancreatic tumor formation. *Cell* **148**, 349–361 (2012).
7. Grünwald, B. et al. Pancreatic premalignant lesions secrete tissue inhibitor of metalloproteinases-1, which activates hepatic stellate cells via CD63 signaling to create a premetastatic niche in the liver. *Gastroenterology* **151**, 1011–1024. e7 (2016).
8. Seubert, B. et al. Tissue inhibitor of metalloproteinases (TIMP)-1 creates a premetastatic niche in the liver through SDF-1/CXCR4-dependent neutrophil recruitment in mice. *Hepatology* **61**, 238–248 (2015).
9. Hoshino, A. et al. Tumour exosome integrins determine organotropic metastasis. *Nature* **527**, 329–335 (2015).
10. Costa-Silva, B. et al. Pancreatic cancer exosomes initiate pre-metastatic niche formation in the liver. *Nat. Cell Biol.* **17**, 816–826 (2015).
11. Kowanetz, M. et al. Granulocyte-colony stimulating factor promotes lung metastasis through mobilization of Ly6G+Ly6C+ granulocytes. *Proc. Natl Acad. Sci. USA* **107**, 21248–21255 (2010).
12. Hiratsuka, S. et al. The S100A8-serum amyloid A3-TLR4 paracrine cascade establishes a pre-metastatic phase. *Nat. Cell Biol.* **10**, 1349–1355 (2008).
13. Hiratsuka, S., Watanabe, A., Aburatani, H. & Maru, Y. Tumour-mediated upregulation of chemoattractants and recruitment of myeloid cells predetermines lung metastasis. *Nat. Cell Biol.* **8**, 1369–1375 (2006).
14. Schmidt-Arras, D. & Rose-John, S. IL-6 pathway in the liver: From physiopathology to therapy. *J. Hepatol.* **64**, 1403–1415 (2016).
15. Long, K. B. et al. IL6 receptor blockade enhances chemotherapy efficacy in pancreatic ductal adenocarcinoma. *Mol. Cancer Ther.* **16**, 1898–1908 (2017).
16. Lesina, M. et al. Stat3/Socs3 activation by IL-6 transsignaling promotes progression of pancreatic intraepithelial neoplasia and development of pancreatic cancer. *Cancer Cell* **19**, 456–469 (2011).
17. Fukuda, A. et al. Stat3 and MMP7 contribute to pancreatic ductal adenocarcinoma initiation and progression. *Cancer Cell* **19**, 441–455 (2011).
18. Corcoran, R. B. et al. STAT3 plays a critical role in KRAS-induced pancreatic tumorigenesis. *Cancer Res.* **71**, 5020–5029 (2011).
19. Eckhardt, E. R. et al. Intestinal epithelial serum amyloid A modulates bacterial growth *in vitro* and pro-inflammatory responses in mouse experimental colitis. *BMC Gastroenterol.* **10**, 133 (2010).
20. Urieli-Shoval, S., Linke, R. P. & Matzner, Y. Expression and function of serum amyloid A, a major acute-phase protein, in normal and disease states. *Curr. Opin. Hematol.* **7**, 64–69 (2000).
21. Notta, F. et al. A renewed model of pancreatic cancer evolution based on genomic rearrangement patterns. *Nature* **538**, 378–382 (2016).
22. Yachida, S. et al. Distant metastasis occurs late during the genetic evolution of pancreatic cancer. *Nature* **467**, 1114–1117 (2010).
23. Reichert, M. et al. Regulation of epithelial plasticity determines metastatic organotropism in pancreatic cancer. *Dev. Cell* **45**, 696–711.e8 (2018).

Competing interests The authors declare no competing interests.

Additional information
Extended data is available for this paper at https://doi.org/10.1038/s41586-019-1004-y.
Supplementary information is available for this paper at https://doi.org/10.1038/s41586-019-1004-y.
Reprints and permissions information is available at http://www.nature.com/reprints.
Correspondence and requests for materials should be addressed to G.L.B.
Publisher's note: Springer Nature remains neutral with regard to jurisdictional claims in published maps and institutional affiliations.

METHODS

Mice. CD45.2 (wild type, C57BL/6J), CD45.1 (B6.SJL-*Ptprc^a Pepc^b*/BoyJ), *Il6* knockout (*Il6^{-/-}*, B6.129S2-*Il6^{tm1Kopf}*/J), *Stat3^{flox/flox}* (B6.129S1-*Stat3^{tm1Xyfu}*/J), and *Alb-cre^{+/+}* (B6.Cg-Tg(Alb-cre)21Mgn/J) mice were obtained from the Jackson Laboratory. *Stat3^{flox/flox}* mice were bred to *Alb-cre^{+/+}* mice to generate *Stat3^{flox/+} Alb-cre^{+/-}* mice, which were backcrossed onto *Stat3^{flox/flox}* mice to generate *Stat3^{flox/flox} Alb-cre^{+/-}* mice. These mice were then bred to each other to create *Stat3^{flox/flox} Alb-cre^{+/+}* and *Stat3^{flox/flox} Albumin-cre^{+/-}* mice (*Stat3^{flox/flox} Alb-cre*), and *Stat3^{flox/flox} Albumin-cre^{-/-}* mice (*Stat3^{flox/flox}*). *Kras^{LSL-G12D/+} Trp53^{LSL-R172H/+} Pdx1-cre* (KPC) mice and *Trp53^{LSL-R172H/+} Pdx1-cre* (PC) mice were as previously described[4,5]. *Saa1* and *Saa2* double-knockout (*Saa^{-/-}*) mice were as previously described[24] and provided by the University of Kentucky College of Medicine. *Saa^{-/-}* mice used for experiments had been bred to obtain a 99.9% C57BL/6 background using the Jackson Laboratory Speed Congenic Service[24]. All transgenic mice were bred and maintained in the animal facility of the University of Pennsylvania. Animal protocols were reviewed and approved by the Institute of Animal Care and Use Committee of the University of Pennsylvania. In general, mice were monitored three times per week for general health and euthanized early based on defined endpoint criteria including tumour diameter ≥1 cm, ascites, lethargy, loss of ≥10% body weight, or other signs of sickness or distress.

Clinical samples. All patient samples were obtained after written informed consent and were de-identified. Studies were conducted in accordance with the 1996 Declaration of Helsinki and approved by institutional review boards of the University of Pennsylvania and the Mayo Clinic. To obtain plasma from healthy donors, patients with PDAC patients, and patients with NSCLC, peripheral whole blood was drawn in EDTA tubes (Fisher Scientific). Within 3 h of collection, blood samples were centrifuged at 1,600*g* at room temperature for 10 min with the brake off. Next, the plasma was transferred to a 15-ml conical tube without disturbing the cellular layer and centrifuged at 3,000*g* at room temperature for 10 min with the brake off. This step was repeated with a fresh 15-ml conical tube. The plasma was then stored at −80 °C until analysis. Biopsy results, computed tomography, and/or magnetic resonance imaging records were used to determine sites of metastasis in patients with PDAC or NSCLC whose plasma samples were used for assessment of SAA levels. Liver specimens from healthy donors were obtained by percutaneous liver biopsy, and acquisition of liver specimens from patients with liver metastases was as previously described[25]. Liver specimens from patients with CRC with liver metastases were obtained from the Cooperative Human Tissue Network (CHTN). Patient characteristics are shown in Supplementary Table 2.

Cell lines. PDA.69 cell line (PDAC cells) was used for intrasplenic and orthotopic injection, and PDA.8572 cell line (PDAC–YFP cells) was used for intrasplenic, intraportal, and retro-orbital injections. These cell lines were derived from PDAC tumours that arose spontaneously in KPC mice, as previously described[4,26]. The MC-38 cell line, which was used for orthotopic implantation, was purchased from Kerafast. Cell lines were cultured in DMEM (Corning) supplemented with 10% fetal bovine serum (FBS, VWR), 83 μg/ml gentamicin (Thermo Fisher), and 1% GlutaMAX (Thermo Fisher) at 37 °C, 5% CO$_2$. Only cell lines that had been passaged fewer than 10 times were used for experiments, and trypan blue staining was used to ensure that cells with >95% viability were used for studies. Cell lines were tested routinely for *Mycoplasma* contamination at the Cell Center Services Facility at the University of Pennsylvania. All cell lines used in our studies tested negative for *Mycoplasma* contamination.

Animal experiments. For all animal studies, mice of similar age and gender were block randomized in an unblinded fashion. Male and female mice aged between 8 to 12 weeks were used unless indicated otherwise. Mice were age- and gender-matched with appropriate control mice for analysis. Sample sizes were estimated based on pilot experiments and were selected to provide sufficient numbers of mice in each group for statistical analysis.

For orthotopic and intrasplenic injections of pancreatic tumour cells, mice were anaesthetized using continuous isoflurane, and their abdomen was sterilized. After administering analgesic agents and assessing the depth of anaesthesia, we performed a laparotomy (5–10 mm) over the left upper quadrant of the abdomen to expose the peritoneal cavity. For orthotopic injection, the pancreas was exteriorized onto a sterile field, and sterile PBS or pancreatic tumour cells (5 × 10^5 cells suspended in 50 μl of sterile PBS) were injected into the tail of the pancreas via a 30-gauge needle (Covidien). Successful injection was confirmed by the formation of a liquid bleb at the site of injection with minimal fluid leakage. The pancreas was then gently placed back into the peritoneal cavity. For intrasplenic injection, 150 μl sterile PBS was drawn into a syringe and then sterile PBS or pancreatic tumour cells (5 × 10^5 cells suspended in 100 μl sterile PBS) was gently drawn into the same syringe in an upright position as previously described[27]. After the spleen was exteriorized onto a sterile field, pancreatic tumour cells were injected into the spleen via a 30-gauge needle. Successful injection was confirmed by whitening of the spleen and splenic blood vessels with minimal leakage of content into the peritoneum. Splenectomy was then performed by ligating splenic vessels with clips (Horizon)

then cauterizing them to ensure that there was no haemorrhage. Afterwards, the remaining blood vessels were placed back into the peritoneal cavity. For both procedures, the peritoneum was closed with a 5-0 PDS II violet suture (Ethicon), and the skin was closed using the AutoClip system (Braintree Scientific). Following surgery, mice were given buprenorphine subcutaneously at a dose of 0.05-0.1 mg/kg every 4–6 h for 12 h and then every 6–8 h for 3 additional days. Mice that were orthotopically injected with pancreatic tumour cells were analysed after 20 days, unless indicated otherwise in study designs. Mice that were intrasplenically injected with PDAC cells were analysed after 10 days.

For intraportal injection of pancreatic tumour cells and hydrodynamic injection of expression vectors, mice were anaesthetized using continuous isoflurane, and their abdomen was sterilized. After administration of analgesic agents, median laparotomy (10 mm) was performed, and the incision site was held open using an Agricola retractor (Roboz). After exposure of the peritoneal cavity, the intestines were located and exteriorized onto a sterile field surrounding the incision site to visualize the portal vein. Throughout the procedure, the intestines were kept hydrated with sterile PBS that was pre-warmed to 37 °C. For intraportal injection, sterile PBS or pancreatic tumour cells (5 × 10^5 cells suspended in 100 μl sterile PBS) were injected into the portal vein via a 30-gauge needle. Successful injection was confirmed by partial blanching of the liver. For hydrodynamic injection, 1 μg of pLIVE expression vectors was suspended in sterile saline corresponding to 8% of mouse body weight as previously described[28]. Vectors were injected into the portal vein via a 27-gauge needle within 5–8 s. Successful injection was confirmed by complete blanching and swelling of the liver. For both procedures, a sterile gauge was then held over the injection site for 1 min to ensure that no injected contents would leak into the peritoneal cavity. Afterwards, the intestines were placed back into the peritoneal cavity, and the peritoneum and skin were closed with a suture and autoclips, respectively. Following surgery, mice were given buprenorphine subcutaneously as described above. Intraportal injection of pancreatic tumour cells was performed on day 10, and metastatic burden in the liver was evaluated on day 20, unless indicated otherwise in study designs.

For orthotopic implantation of colorectal tumour cells, wild-type mice were first subcutaneously injected with MC-38 (1 × 10^6 cells suspended in 100 μl of sterile PBS) into the right flank. After 10 days, mice were euthanized, and subcutaneous tumours were collected. Tumours were then cut into small pieces, each 3 × 3 mm in size, and placed in sterile PBS on ice until implantation. Mice were anaesthetized using isoflurane, and their abdomen was sterilized. Following administration of analgesic agents, median laparotomy was performed as described above. Implantation of colorectal tumour tissues into the caecum was then performed as previously described[29]. After we placed the intestines back into the peritoneal cavity, the peritoneum and skin were closed with a suture, and mice were given buprenorphine as described above. Mice were analysed after 10 days.

For parabiotic joining of mice, female CD45.2 mice were orthotopically injected with sterile PBS or pancreatic tumour cells as described above and co-housed with age-matched female B6 CD45.1 mice. Each parabiotic pair was housed in a separate cage to maximize bonding between partners. After one week, parabiotic partners were anaesthetized using continuous isoflurane, and their flanks were sterilized. After administration of analgesic agents, longitudinal skin flaps from the lower limb to the upper limb were created, and everted skin flaps were sewn using a suture. In addition, the knees and olecranons of parabiotic partners were joined together using a suture for additional stabilization. Following surgery, mice were given buprenorphine subcutaneously at a dose of 0.05-0.1 mg/kg every 4-6 h for 5 days. Parabiotically joined mice were analysed after 20 days.

For administration of antibodies, the abdomen of mice was sterilized, and anti-CD4 antibodies (GK1.5, 0.2 mg), anti-CD8 antibodies (2.43, 0.2 mg), anti-IL-6R antibodies (15A7, 0.2 mg), or rat isotype control antibodies (LTF-2, 0.2 mg) were suspended in 100 μl sterile PBS. Antibodies were subsequently injected into the peritoneum via a 30-gauge needle. All antibodies used in in vivo experiments were obtained from BioXCell. To deplete F4/80^+ myeloid cells, clodronate-encapsulated liposomes (Liposoma) were administered by intraperitoneal injection according to the manufacturer's protocol. For induction of liver injury, mice were intraperitoneally injected with CCl$_4$ (Sigma, 1 ml/kg body weight) dissolved in sunflower seed oil as previously described[30]. Detailed information on antibodies and reagents used in experiments can be in found in Supplementary Table 3.

Microscopic analysis. For preparation of formalin-fixed paraffin-embedded (FFPE) sections, dissected tissues were fixed in 10% formalin for 24 h at room temperature, washed twice with PBS, and then stored in 70% ethanol solution at 4 °C until they were embedded in paraffin and sectioned at 5 μm. For preparation of cryosections, dissected tissues were embedded in Tissue-tek O.C.T. (Electron Microscopy Sciences) and frozen on dry ice. Frozen tissues were stored at −80 °C until they were sectioned at 7 μm.

Automated immunohistochemistry, immunofluorescence, and RNA in situ hybridization were performed on FFPE sections using a Ventana Discovery Ultra

automated slide staining system (Roche). Reagents were obtained from Roche and ACDBio (Supplementary Table 3) and used according to manufacturer's protocol. Images were acquired using a BX43 upright microscope (Olympus), an Aperio CS2 scanner system (Leica), or an IX83 inverted multicolour fluorescent microscope (Olympus). Manual immunohistochemistry of mouse tissues for SAA was previously described[31]. For manual multicoloured immunofluorescence staining, O.C.T. liver cryosections were briefly air dried and fixed with 3% formaldehyde at room temperature for 15 min. For intracellular staining, sections were permeabilized with methanol at –20 °C for 10 min immediately after formaldehyde fixation. Sections were then blocked with 10% normal goat serum in PBS containing 0.1% TWEEN 20 for 30 min. For intracellular staining, 0.3% Triton X-100 was added to the blocking solution for permeabilization of cellular and nuclear membranes. Sections were incubated with primary antibodies (Supplementary Table 3) in the blocking solution for 1 h at room temperature or overnight at 4 °C, followed by washing with PBS containing 0.1% TWEEN 20. Sections were then incubated with secondary antibodies (Supplementary Table 3) in the blocking solution for 1 h at room temperature or overnight at 4 °C. After washing, sections were stained with DAPI to visualize nuclei and subsequently with Sudan Black B in 70% ethanol to reduce autofluorescence, as previously described[32]. Immunofluorescence imaging was performed on an IX83 inverted multicolour fluorescent microscope (Olympus). For quantification of cells and extracellular matrix proteins, five random fields were acquired from each biological sample.

Flow cytometry. Mice were euthanized, and the liver and lung were removed after the blood was drained by severing the portal vein and inferior vena cava. The liver and lung were rinsed thoroughly in PBS before mincing with micro-dissecting scissors into small pieces ($<0.5 \times 0.5$ mm in size) at 4 °C in DMEM containing collagenase (1 mg/ml, Sigma-Aldrich), DNase (150 U/ml, Roche), and Dispase (1 U/ml, Worthington). Tissues were then incubated at 37 °C for 30 min with intermittent agitation, filtered through a 70-μm nylon strainer (Corning), and washed three times with DMEM. Cells were resuspended in ACK lysing buffer (Life Technologies) at room temperature for 15 min to remove red blood cells. After washing three times with DMEM, cells were counted and stained using Aqua dead cell stain kit (Life Technologies) following the manufacturer's protocol. For characterization of immune cell subsets, cells were washed three times with PBS containing 0.2 mM EDTA with 2% FBS and stained with appropriate antibodies (Supplementary Table 3). For quantification of PDAC–YFP cells, cells were not stained with any antibodies. Lastly, cells were washed three times with PBS containing 0.2 mM EDTA with 2% FBS and examined using a FACS Canto II (BD Biosciences). Collection and analysis of the peripheral blood was as previously described[26]. FlowJo (FlowJo, LLC, version 10.2) was used to analyse flow cytometric data and generate 2D t-SNE plots.

Detection of IL-6, SAA, and TIMP1. Mice that were orthotopically implanted with PDAC cells were euthanized, and primary tumours were removed and weighed. In addition, blood samples were collected from the portal vein and left ventricle of the heart using a 27-gauge needle. Tumours were rinsed thoroughly in PBS and minced with micro-dissecting scissors into small pieces ($<0.5 \times 0.5$ mm in size) at 4 °C in serum-free DMEM at 1 mg of tissue per 1 μl medium. Tumour suspensions were then centrifuged at $12,470g$ at 4 °C for 15 min, and tumour supernatant was collected and stored at –80 °C until analysis. A similar procedure was performed to obtain pancreas supernatant from mice that were orthotopically injected with PBS. To collect the serum, blood samples were allowed to clot at room temperature for 30 min. Samples were then centrifuged at $12,470g$ at 4 °C for 15 min, and the serum was collected and stored at –80 °C until analysis. IL-6 levels in tumour or pancreas supernatant and serum were assessed using a cytometric bead array (BD Biosciences) following the manufacturer's protocol. Samples were examined using a FACS Canto II (BD Biosciences), and data were analysed using FCAP Array (BD Biosciences, version 3.0). SAA and TIMP1 levels in mouse serum samples were measured using a commercially available enzyme-linked immunosorbent assay kit (Thermo Fisher) following the manufacturer's protocol. Similarly, SAA levels in plasma samples collected from healthy donors and patients with PDAC as described under 'Clinical samples' were measured using a commercially available human enzyme-linked immunosorbent assay kit (Thermo Fisher) following the manufacturer's protocol.

RNA and quantitative PCR. Mouse organs and cells were stored in TRIzol (Thermo Fisher) at –80 °C until analysis. Samples were thawed on ice and allowed to equilibrate to room temperature before RNA was isolated using a RNeasy Mini kit (Qiagen) following the manufacturer's protocol. cDNA synthesis was performed as previously described[33]. Primers for quantitative PCR were designed using the Primer3 online program[34], and sequences were analysed using the Nucleotide BLAST (NCBI) to minimize non-specific binding of primers. Primers were synthesized by Integrated DNA Technologies, and their sequences can be found in Supplementary Table 4. Quantitative PCR was performed as previously described[33]. Gene expression was calculated relative to *Actb* (β-actin) using the ΔC_t formula, and fold change in gene expression was calculated relative to the average gene expression of control groups using the $\Delta\Delta C_t$ formula. Genes with C_t greater than or equal to 30 were considered not detected.

QuantSeq 3′ mRNA sequencing and data analysis. RNA was isolated from the livers of control mice and NTB KPC mice as described above and submitted to the Genomics Facility at the Wistar Institute. After the quality of RNA was assessed using a 2100 Bioanalyzer (Agilent), samples were prepared using a QuantSeq 3′ mRNA-Seq library prep kit FWD for Illumina (Lexogen) following the manufacturer's protocol and analysed on a NextSeq 500 sequencing system (Illumina). FASTQ files were uploaded to the BaseSpace Suite (Illumina) and aligned using its RNA-Seq Alignment application (version 1.0.0), in which STAR was selected to align sequences with maximum mismatches set to 14 as recommended by Lexogen. Output files were analysed using Cufflinks Assembly & DE application (version 2.1.0) in the BaseSpace Suite to determine differentially expressed genes, which were used to generate an expression heatmap and a FPKM scatter plot. In addition, these genes were analysed using ClueGO (version 2.3.3)[35] and CluePedia (version 1.3.3)[36], which are applications of Cytoscape software (version 3.5.1)[37]. Functional grouping of biological processes was performed on the basis of kappa score. Gene Ontology data[38,39] downloaded on 23 January 2018 were used for analysis. Gene set enrichment analysis (version 3.0)[40] was used to determine biological processes that were differentially enriched in experimental groups.

In vitro studies. To isolate primary hepatocytes for in vitro studies, mice were anaesthetized using continuous isoflurane, and their abdomen was sterilized. After administering analgesic agents and assessing the depth of anaesthesia, we performed a laparotomy (10–15 mm) along the midline of the abdomen to expose the peritoneal cavity. The intestines were then located and exteriorized to visualize the inferior vena cava and portal vein. The inferior vena cava was cannulated via a 24 gauge Insyte Autoguard catheter (BD), and the liver was perfused using 50 ml liver perfusion medium (Thermo Fisher) at a flow rate of 8–9 ml/min using a peristaltic pump. At the start of perfusion, the portal vein was severed to drain the blood from the liver. Successful perfusion was confirmed by blanching of the liver, which was subsequently perfused using 50 ml liver digest medium (Thermo Fisher) at the same flow rate. Both liver perfusion medium and liver digest medium were pre-warmed to 42 °C in a water bath. After perfusion, the liver was carefully transferred to a Petri dish containing William's E medium (Sigma) supplemented with 10% FBS, 83 μg/ml gentamicin, and 1% GlutaMAX.

To dissociate hepatocytes from the liver, cell scrapers were used to create small cuts (5 mm) on the surface of the liver, and the tissue was gently shaken. Dissociated cells were then filtered through a 100-μm nylon strainer (Corning) and centrifuged at $50g$ at 4 °C for 5 min. After the supernatant was discarded, cells were resuspended in a solution consisting of isotonic Percoll (Sigma) and supplemented William's E medium (2:3 ratio). Cells were then centrifuged at $50g$ at 4 °C for 10 min to obtain a pellet enriched in hepatocytes. The supernatant was discarded, and hepatocytes were resuspended in supplemented William's E medium. Cell viability and number were determined using trypan blue staining, and 5×10^4 hepatocytes were seeded in each well of a 48-well plate pre-coated with collagen. Hepatocytes were incubated in supplemented William's E medium for 4 h at 37 °C, 5% CO_2 to allow attachment to the plate. The medium was then switched to HepatoZYME-SFM (Thermo Fisher) supplemented with 83 μg/ml gentamicin and 1% GlutaMAX. Medium was replenished every 24 h for the next 48–72 h.

For hepatocyte activation assays, hepatocytes were incubated in supplemented HepatoZYME-SFM mixed with (i) serum-free DMEM, (ii) primary pancreatic tumour supernatant, or (iii) serum-free DMEM containing 250 ng/ml IL-6 (Peprotech) for 30 min at 37 °C, 5% CO_2. All mixtures were made in a 1:1 ratio, and each condition was run in triplicate. For the in vitro IL-6R blockade experiment, hepatocytes were pre-incubated with 5 μg/ml anti-IL-6R antibodies for 2 h before being stimulated with tumour supernatant. After stimulation, medium was carefully removed, and formaldehyde and methanol were used to fix and permeabilize hepatocytes, respectively, as described above. Hepatocytes were then stained for pSTAT3 (Supplementary Table 3), and their nuclei stained with DAPI. Immunofluorescence imaging was performed on an IX83 inverted multicolour fluorescent microscope (Olympus).

Statistical analysis. Statistical significance was calculated using Prism (GraphPad Software, version 7) unless indicated otherwise. Multiple comparisons testing was performed using one-way ANOVA with Dunnett's test. Paired group comparisons test was carried out using two-tailed Wilcoxon matched-pairs signed rank test. Unpaired group comparisons test was performed using two-tailed unpaired Student's t test or two-tailed Mann–Whitney test. Comparison of Kaplan–Meier overall survival curves was performed using log-rank (Mantel–Cox) test. P values less than 0.05 were treated as significant. The experiments were not randomized and the investigators were not blinded to allocation during experiments and outcome assessment, unless stated otherwise.

Reporting summary. Further information on research design is available in the Nature Research Reporting Summary linked to this paper.

Data availability

QuantSeq 3′ mRNA sequencing data have been deposited in the Gene Expression Omnibus (GEO) under accession number GSE109480. Source Data are provided for all figures and extended data figures. All data are available from the corresponding author upon reasonable request.

24. de Beer, M. C. et al. Impact of serum amyloid A on high density lipoprotein composition and levels. *J. Lipid Res.* **51**, 3117–3125 (2010).
25. Liang, W. S. et al. Genome-wide characterization of pancreatic adenocarcinoma patients using next generation sequencing. *PLoS One* **7**, e43192 (2012).
26. Long, K. B. et al. IFNγ and CCL2 cooperate to redirect tumor-infiltrating monocytes to degrade fibrosis and enhance chemotherapy efficacy in pancreatic carcinoma. *Cancer Discov.* **6**, 400–413 (2016).
27. Soares, K. C. et al. A preclinical murine model of hepatic metastases. *J. Vis. Exp.* **91**, 51677 (2014).
28. Ma, Y., Gao, M., Sun, H. & Liu, D. Interleukin-6 gene transfer reverses body weight gain and fatty liver in obese mice. *Biochim. Biophys. Acta* **1852**, 1001–1011 (2015).
29. Tseng, W., Leong, X. & Engleman, E. Orthotopic mouse model of colorectal cancer. *J. Vis. Exp.* **10**, 484 (2007).
30. Klaas, M. et al. The alterations in the extracellular matrix composition guide the repair of damaged liver tissue. *Sci. Rep.* **6**, 27398 (2016).
31. Webb, N. R. et al. Deficiency of endogenous acute-phase serum amyloid A protects apoE−/− mice from angiotensin II-induced abdominal aortic aneurysm formation. *Arterioscler. Thromb. Vasc. Biol.* **35**, 1156–1165 (2015).
32. Sun, Y. et al. Sudan black B reduces autofluorescence in murine renal tissue. *Arch. Pathol. Lab. Med.* **135**, 1335–1342 (2011).
33. Kalbasi, A. et al. Tumor-derived CCL2 mediates resistance to radiotherapy in pancreatic ductal adenocarcinoma. *Clin. Cancer Res.* **23**, 137–148 (2017).
34. Untergasser, A. et al. Primer3—new capabilities and interfaces. *Nucleic Acid Res.* **40**, e115 (2012).
35. Bindea, G. et al. ClueGO: a Cytoscape plug-in to decipher functionally grouped gene ontology and pathway annotation networks. *Bioinformatics* **25**, 1091–1093 (2009).
36. Bindea, G., Galon, J. & Mlecnik, B. CluePedia Cytoscape plugin: pathway insights using integrated experimental and in silico data. *Bioinformatics* **29**, 661–663 (2013).
37. Shannon, P. et al. Cytoscape: a software environment for integrated models of biomolecular interaction networks. *Genome Res.* **13**, 2498–2504 (2003).
38. The Gene Ontology Consortium. Expansion of the Gene Ontology knowledgebase and resources. *Nucleic Acids Res.* **45**, D331–D338 (2017).
39. Ashburner, M. et al. Gene ontology: tool for the unification of biology. *Nat. Genet.* **25**, 25–29 (2000).
40. Subramanian, A. et al. Gene set enrichment analysis: a knowledge-based approach for interpreting genome-wide expression profiles. *Proc. Natl Acad. Sci. USA* **102**, 15545–15550 (2005).
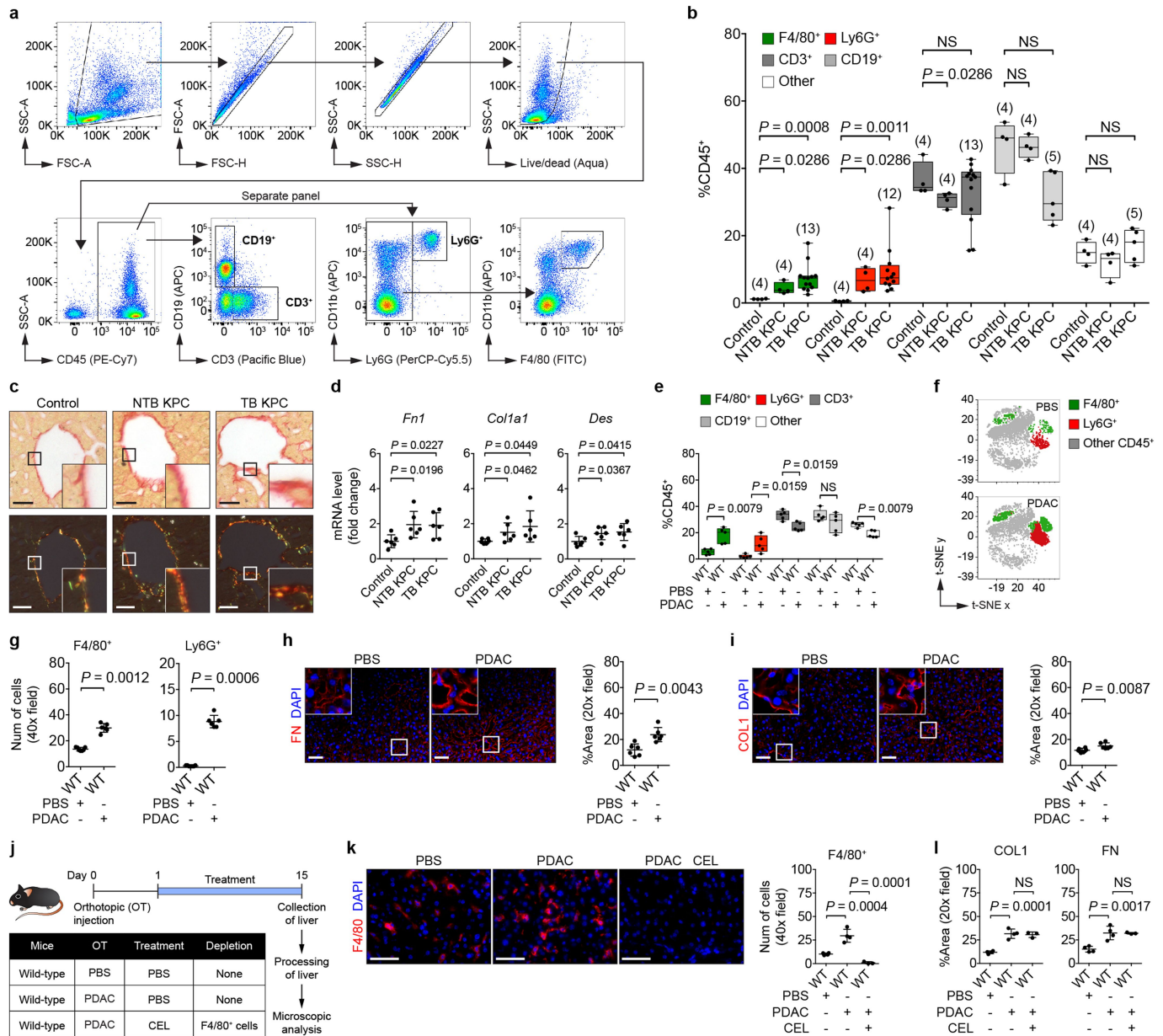
Extended Data Fig. 1 | Primary PDAC development induces myeloid cell accumulation and fibrosis within the liver. a, Gating strategy for identification of F4/80^{+}, Ly6G^{+}, CD3^{+}, and CD19^{+} cells. Representative images from flow cytometric analysis of cells isolated from the liver of a tumour-bearing KPC mouse are shown. **b**, Quantification of immune cells in the liver by flow cytometry. Numbers in parentheses indicate the number (n) of mice. Data pooled from four experiments. **c**, Representative Sirius red staining of the liver ($n = 5$ for all groups) viewed using standard light microscopy (top) and polarized light (bottom). **d**, mRNA levels of *Fn1*, *Col1a1*, and *Des* in the liver ($n = 6$ for all groups). Data pooled from two experiments (**c, d**). **e–i**, Wild-type mice were orthotopically injected with PBS or PDAC cells and analysed on day 20. **e**, Quantification of immune cells in the liver by flow cytometry ($n = 5$ for both groups). **f**, *t*-distributed stochastic neighbour embedding (*t*-SNE) 2D plots of immune cells analysed in **e**. **g**, Quantification of myeloid cells in the liver

($n = 7$ for PBS and $n = 6$ for PDAC). **h, i**, Images and quantification of fibronectin and COL1 in the liver ($n = 6$ for both groups). Data representative of at least two independent experiments (**e–i**). **j**, Study design for **k** and **l** ($n = 4$ for mice injected with PBS; $n = 4$ and 3 for mice injected with PDAC cells and then intraperitoneally injected with PBS and clodronate-encapsulated liposomes (CEL), respectively). **k**, Images and quantification of F4/80^{+} cells in the liver. **l**, Quantification of COL1 and fibronectin in the liver. Data representative of one experiment (**j–l**). Scale bars, 100 μm (**c**) and 50 μm (other panels). Statistical significance calculated using two-tailed unpaired Student's *t*-test (**d**), one-way ANOVA with Dunnett's test (**k, l**), and two-tailed Mann–Whitney test (other panels). NS, not significant. Data represented as mean ± s.d., except **b** and **e**, which are shown as box plots (centre line, median; box limits, upper and lower quartiles; whiskers, maximum and minimum values).
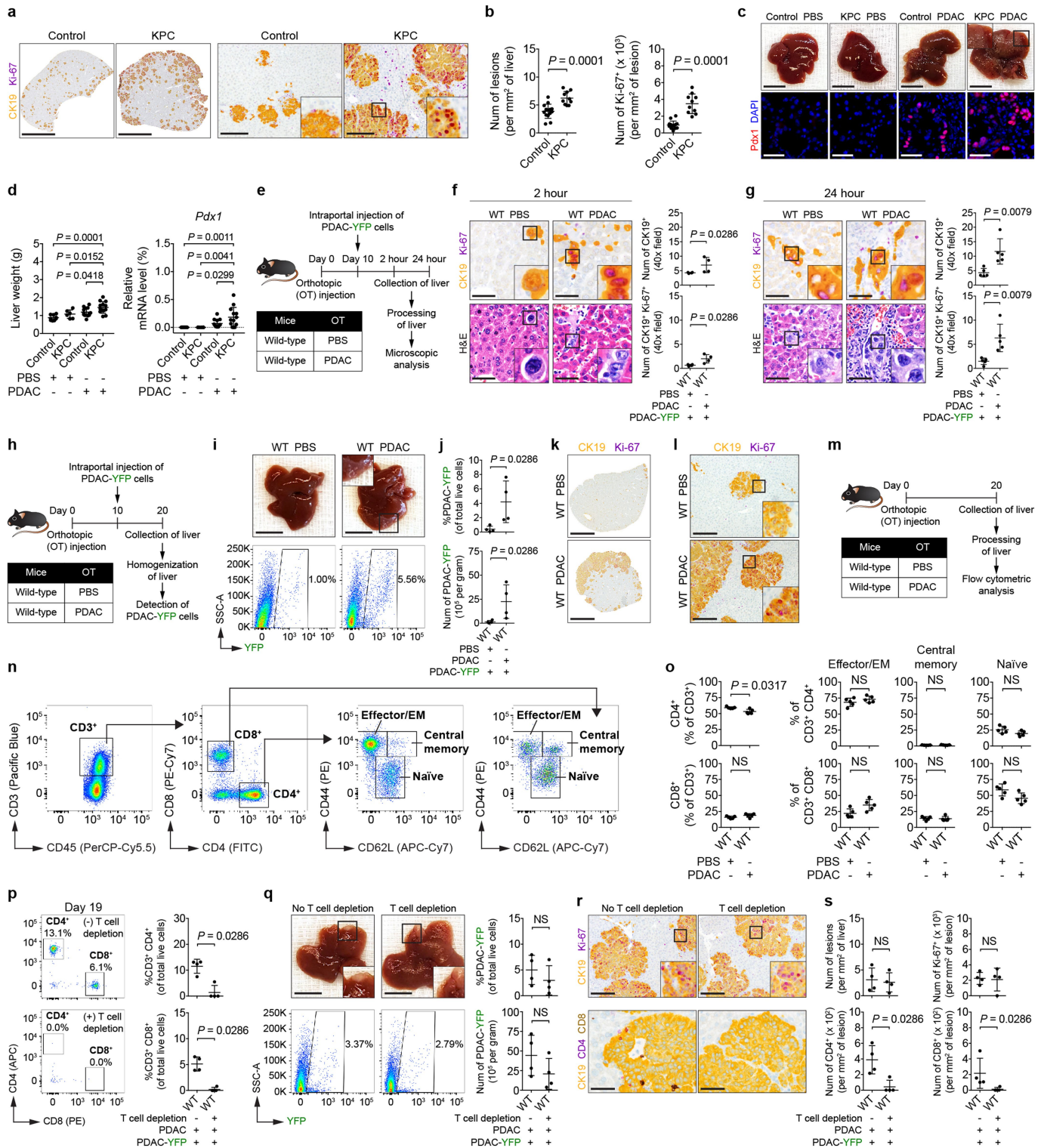
Extended Data Fig. 2 | See next page for caption.

Extended Data Fig. 2 | Primary PDAC development enhances liver susceptibility to metastatic colonization. a, b, Control mice ($n = 14$) and NTB KPC mice ($n = 10$) were intrasplenically injected with PDAC–YFP cells, and the liver was analysed after 10 days. **a**, Images of the liver showing metastatic lesions (yellow, CK19) and Ki-67 (purple). Scale bars, 4 mm (left) and 200 μm (right). **b**, Quantification of lesions (left) and Ki-67$^+$ tumour cells (right). Data pooled from three experiments (**a, b**). **c, d**, $n = 9$ and 13 for control mice and $n = 6$ and 13 for NTB KPC mice intrasplenically injected with PBS and PDAC (PDA.69), respectively. **c**, Images of the liver (top) and metastatic lesions in the liver (stained with PDX1). Scale bars, 1 cm (top) and 50 μm (bottom). **d**, Liver weights and mRNA levels of *Pdx1* in the liver relative to *Gapdh*. Data pooled from five experiments (**c, d**). **e**, Study design for **f** and **g**. Wild-type mice were injected with PBS or PDAC cells and then injected with PDAC–YFP cells on day 10. The liver was removed 2 h (**f**, $n = 4$ for both groups) or 24 h (**g**, $n = 5$ for both groups) after intraportal injection. **f, g**, Images and quantification of tumour cells in the liver. Scale bars, 50 μm. Data representative of one experiment (**e–g**). **h**, Study design for **i–l** ($n = 4$ for both groups). **i**, Images of the liver and flow cytometric analysis. Scale bars, 1 cm. **j**, Quantification of PDAC–YFP cells. **k, l**, Images of the liver showing metastatic lesions (yellow, CK19) and Ki-67 (purple). Scale bars,

4 mm (**k**) and 200 μm (**l**). Data representative of at least three independent experiments (**h–l**). **m**, Study design for **n** and **o** ($n = 5$ for both groups). **n**, Gating strategy for identification of T cell subsets. Images from flow cytometric analysis of cells isolated from the liver of a wild-type mouse are shown. EM, effector memory. **o**, Quantification of CD4$^+$ T cell subsets (top) and CD8$^+$ T cell subsets (bottom) in the liver. Data representative of two independent experiments (**m–o**). **p–s**, Wild-type mice were orthotopically injected with PBS or PDAC cells ($n = 4$ for both groups). One group received anti-CD4 and anti-CD8 antibodies on days 8 and 13. Both groups were intraportally injected with PDAC–YFP cells on day 10. **p**, Flow cytometric analysis of peripheral blood and quantification of CD4$^+$ and CD8$^+$ T cells. **q**, Images of the liver, flow cytometric analysis, and quantification of PDAC–YFP cells. Scale bars, 1 cm. **r**, Images of the liver showing metastatic lesions (yellow, CK19), Ki-67 (purple, top), and CD4$^+$ cells (purple, bottom) and CD8$^+$ cells (brown, bottom). Scale bars, 200 μm (top) and 50 μm (bottom). **s**, Quantification of lesions and Ki-67$^+$ tumour cells (top) and CD4$^+$ cells and CD8$^+$ cells (bottom). Data representative of one experiment (**p–s**). Statistical significance calculated using one-way ANOVA with Dunnett's test (**d**) or two-tailed Mann–Whitney test (other panels). NS, not significant. Data represented as mean ± s.d.
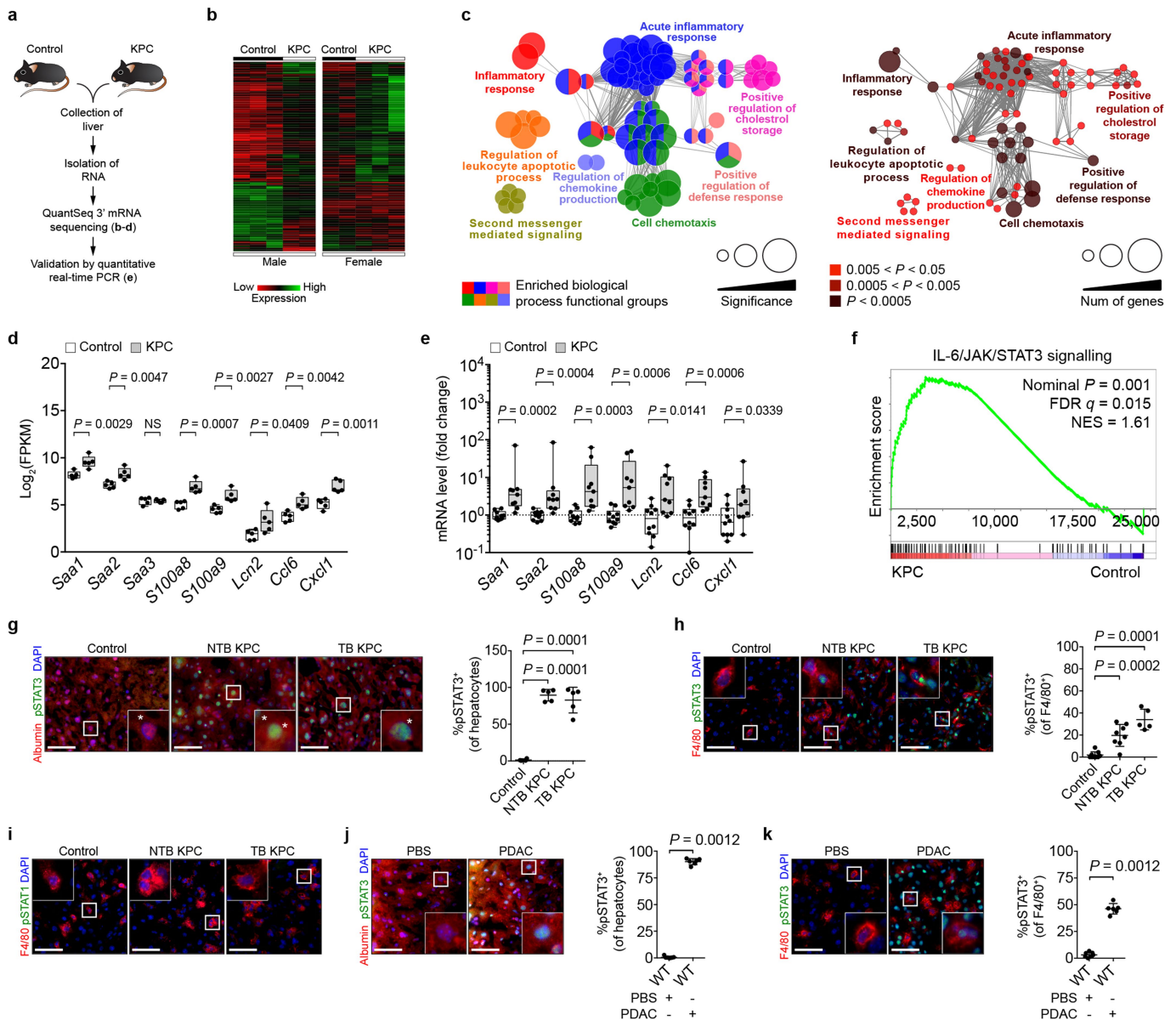
Extended Data Fig. 3 | Primary PDAC development induces expression of myeloid chemoattractants and activates STAT3 signalling in the liver. a, Study design for **b–e** ($n = 5$ for both groups for **b–d** and $n = 10$ and 9 for control mice and NTB KPC mice, respectively, for **e**). **b**, Heat map showing differentially expressed genes in the liver. **c**, Enriched biological processes in the liver of NTB KPC mice. Left, significance; right, number of genes in each group. **d**, FPKM values for chemoattractant genes in the liver. **e**, mRNA levels of chemoattractant genes in the liver. Data representative of one experiment (**a–e**). **f**, Enrichment of IL-6–JAK–STAT3 signalling genes in the liver ($n = 5$ for control mice and NTB KPC mice). FDR, false discovery rate; NES, normalized enrichment score. Data representative of one experiment. **g**, Left, images showing hepatocytes (stained for albumin) and pSTAT3. Right, percentage of hepatocytes that were pSTAT3$^+$ in control mice ($n = 4$), NTB KPC mice ($n = 5$), and TB KPC mice ($n = 5$).

h, Left, images of F4/80$^+$ cells and pSTAT3. Right, percentage of F4/80$^+$ cells that were pSTAT3$^+$ in control mice ($n = 9$), NTB KPC mice ($n = 8$), and TB KPC mice ($n = 5$). **i**, Images of F4/80$^+$ cells and pSTAT1 in the liver of control mice ($n = 9$), NTB KPC mice ($n = 8$), and TB KPC mice ($n = 5$). Data pooled from two experiments (**g–i**). **j**, **k**, Wild-type mice were orthotopically injected with PBS ($n = 7$) or PDAC cells ($n = 6$). Left, images of hepatocytes (**j**), F4/80$^+$ cells (**k**), and pSTAT3. Right, percentage of hepatocytes (**j**) and F4/80$^+$ cells (**k**) that are pSTAT3$^+$. Scale bars, 50 μm. Statistical significance calculated using ClueGO[35] (**c**), two-tailed unpaired Student's t-test (**d**), GSEA[40] (**f**), one-way ANOVA with Dunnett's test (**g**, **h**), and two-tailed Mann–Whitney test (other panels). NS, not significant. Data represented as mean ± s.d., except **d**, **e**, which are shown as box plots (centre line, median; box limits, upper and lower quartiles; whiskers, max and min values).
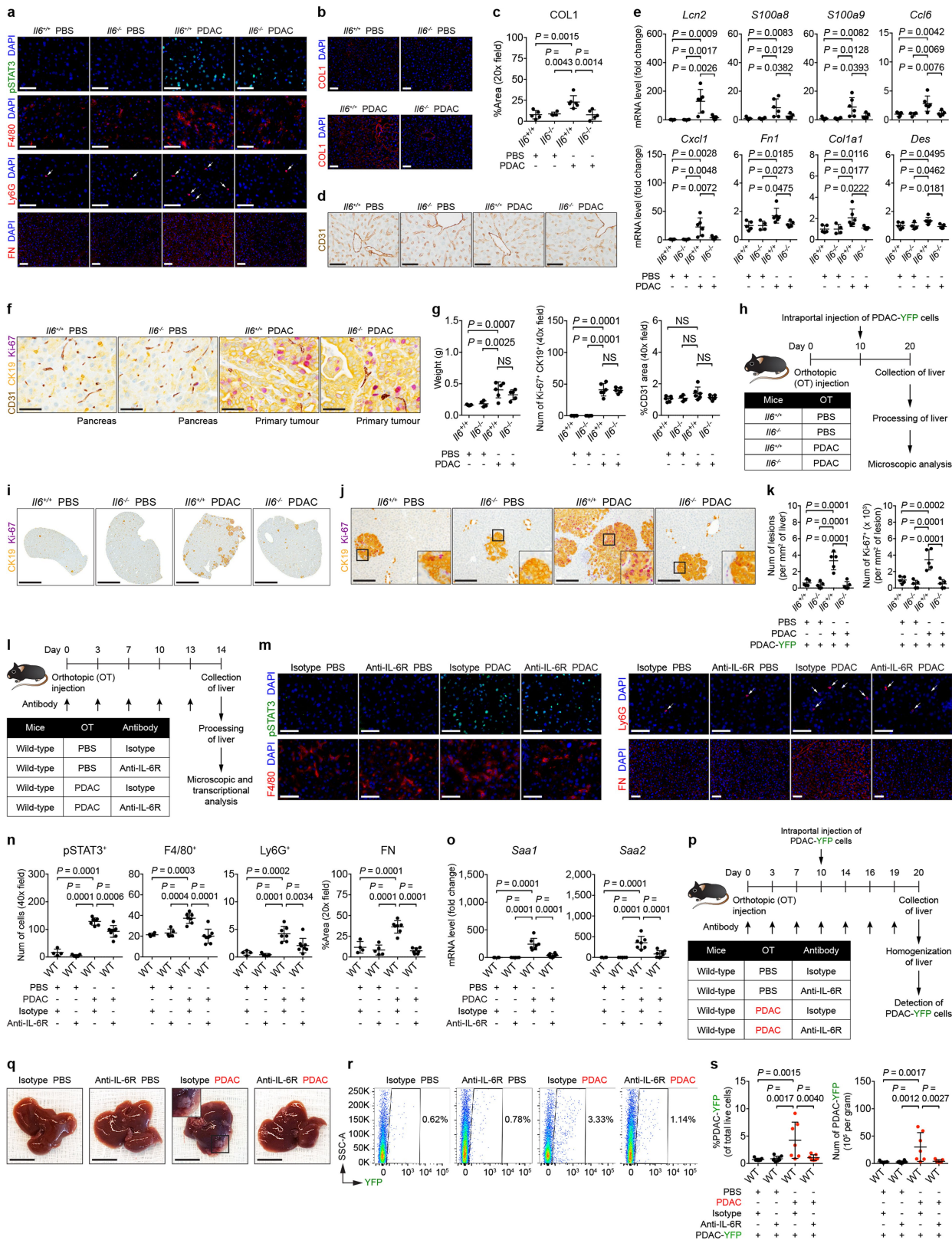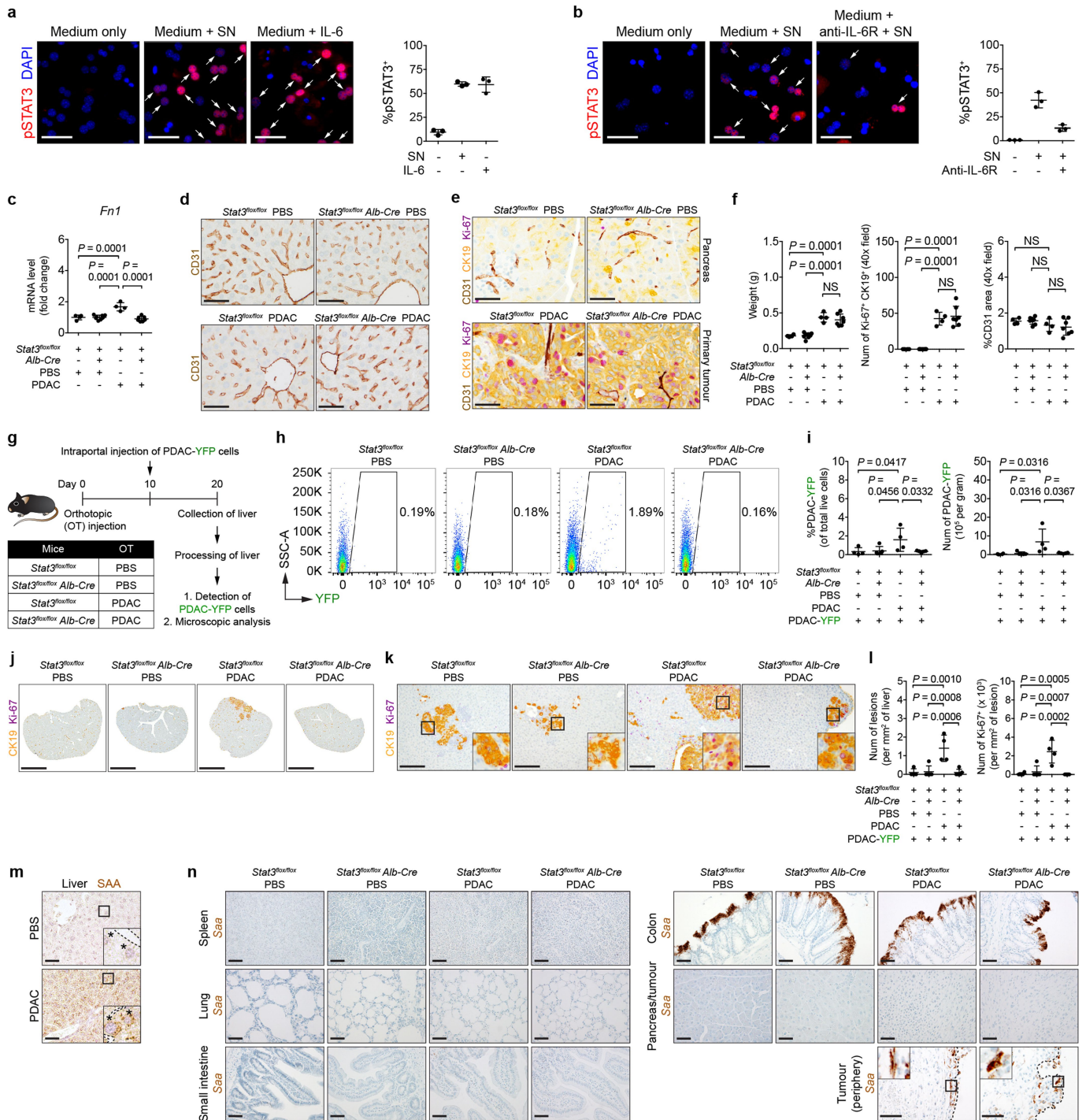
Extended Data Fig. 4 | IL-6 promotes the formation of a pro-metastatic niche in the liver. a–g, $n = 5$ and 6 for $Il6^{+/+}$ mice and $n = 4$ and 5 for $Il6^{-/-}$ mice orthotopically injected with PBS and PDAC cells, respectively. **a,** Images of pSTAT3$^+$ cells, myeloid cells, and fibronectin. Arrows indicate Ly6G$^+$ cells. **b, c,** Images and quantification of COL1. **d,** Images of sinusoids (brown, stained with CD31) in the liver. **e,** mRNA levels of *Lcn2*, *S100a8*, *S100a9*, *Ccl6*, *Cxcl1*, *Fn1*, *Col1a1*, and *Des* in the liver. **f,** Images of pancreas and primary tumour stained with CD31 (brown), CK19 (yellow), and Ki-67 (purple). **g,** Quantification of the weight of pancreas or primary tumour (left), number of Ki-67$^+$ tumour cells (middle), and vascular area (right). Data representative of one (**b–d**, *Fn1*, *Col1a1*, and *Des* in **e–g**) or two independent experiments (**a**, all other genes in **e**). **h,** Study design for **i–k** ($n = 5$ for all groups). All groups were injected with PDAC–YFP cells on day 10. **i, j,** Images of the liver showing metastatic lesions (yellow, CK19) and Ki-67 (purple). Scale bars, 4 mm (**i**) and 200 μm (**j**). **k,** Quantification of lesions (left) and Ki-67$^+$ tumour cells (right). Data representative of one experiment (**h–k**). **l,** Study design for

m–o ($n = 4$ and 5 for mice injected with PBS and treated with isotype control or anti-IL-6R antibodies, respectively; $n = 7$ and 8 for mice injected with PDAC cells and treated with isotype control or anti-IL-6R antibodies, respectively, unless indicated otherwise below). **m, n,** Images and quantification of pSTAT3$^+$ cells, myeloid cells, and fibronectin. For fibronectin, $n = 7$ for mice injected with PDAC cells and treated with anti-IL-6R antibodies. Arrows indicate Ly6G$^+$ cells. **o,** mRNA levels of *Saa1* and *Saa2*. **p,** Study design for **q–s** ($n = 7$ and 8 for mice injected with PBS and treated with isotype control and anti-IL-6R antibodies, respectively; $n = 7$ for mice injected with PDAC cells and treated with isotype control and anti-IL-6R antibodies). All groups were injected with PDAC–YFP cells on day 10. **q, r,** Images of the liver and flow cytometric analysis. Scale bars, 1 cm. **s,** Quantification of PDAC–YFP cells. Data representative of two independent experiments (**l–s**). Scale bars, 50 μm unless indicated otherwise. Statistical significance calculated using one-way ANOVA with Dunnett's test. NS, not significant. Data represented as mean ± s.d.
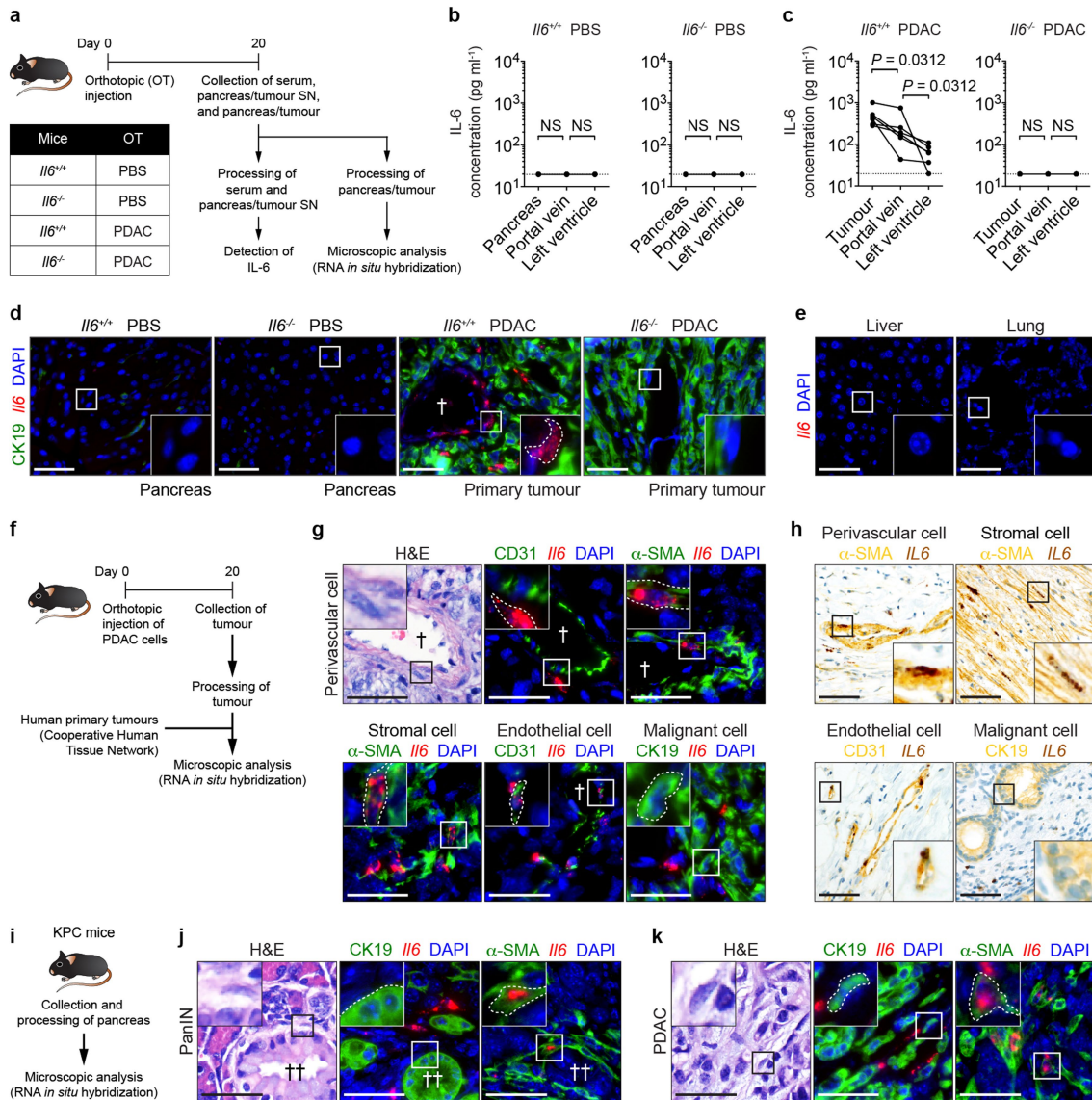
Extended Data Fig. 5 | Non-malignant cells are the predominant source of IL-6. a, Study design for **b**–**e** ($n = 5$ and 6 for $Il6^{+/+}$ mice injected with PBS and PDAC cells, respectively; $n = 4$ and 5 for $Il6^{-/-}$ mice injected with PBS and PDAC cells, respectively). SN, supernatant. **b**, Concentration of IL-6 in pancreas supernatant and serum collected from indicated sites in $Il6^{+/+}$ mice injected with PBS or PDAC cells. **c**, Concentration of IL-6 in pancreatic tumour supernatant and serum collected from indicated sites in $Il6^{-/-}$ mice injected with PBS or PDAC cells. Solid lines indicate data points from individual mice, and dashed lines indicate the lower limit of detection (**b**, **c**). **d**, Images of CK19 and $Il6$ mRNA in the pancreas and primary tumour. **e**, Images of $Il6$ mRNA in the liver and lung of $Il6^{+/+}$ mice injected with PDAC cells. Data representative of two independent experiments (**a**–**e**). **f**, Study design for **g** and **h** ($n = 4$ for $Il6^{+/+}$ mice injected with PDAC cells and $n = 5$ for human samples). **g**, Images of

α-SMA, CD31, CK19, and $Il6$ mRNA in perivascular cells (top), stromal cells (bottom, left), endothelial cells (bottom, middle) and malignant cells (bottom, right) present within the mouse primary tumour. **h**, Images of α-SMA (yellow), CD31 (yellow), CK19 (yellow), and $IL6$ mRNA (brown) in perivascular cells (top, left), stromal cells (top, right), endothelial cells (bottom, left) and malignant cells (bottom, right) present within the human primary tumour. Data representative of one experiment (**f**–**h**). **i**, Study design for **j** and **k** ($n = 5$). **j**, **k**, Representative images of α-SMA, CK19, and $Il6$ mRNA detected in PanIN (**j**) and invasive PDAC (**k**). Data representative of one experiment (**i**–**k**). Scale bars, 50 μm. Statistical significance calculated using two-tailed Wilcoxon test. NS, not significant. Dagger, blood vessel; double dagger, PanIN lesion. Data from individual mice shown in **b**, **c**.

Extended Data Fig. 6 | STAT3 signalling in hepatocytes promotes the formation of a pro-metastatic niche in the liver. a, b, Representative images and quantification of pSTAT3[+] hepatocytes ($n = 3$ technical replicates per condition) treated with or without IL-6 (**a**) or anti-IL-6R (**b**). Arrows indicate pSTAT3[+] hepatocytes. SN, pancreatic tumour supernatant. Data representative of two independent experiments. For **c–f** and **n**, $n = 4$ for *Stat3$^{flox/flox}$* mice and $n = 8$ and 7 for *Stat3$^{flox/flox}$ Alb-cre* mice orthotopically injected with PBS or PDAC cells, respectively. **c**, mRNA levels of *Fn1* in the liver. **d**, Images of sinusoids (brown, stained for CD31) in the liver. **e**, Images of pancreas and primary tumour stained for CD31 (brown), CK19 (yellow), and Ki-67 (purple). **f**, Quantification of the weight of pancreas or primary tumour (left), number of Ki-67^{+} tumour cells (middle), and vascular area (right). Data representative of one experiment (**c–f**). **g**, Study design for **h–l** ($n = 4$ and 5 for *Stat3$^{flox/flox}$* mice

and *Stat3$^{flox/flox}$ Alb-cre* mice, respectively). All groups were injected with PDAC–YFP cells on day 10. **h**, Flow cytometric analysis. **i**, Quantification of PDAC–YFP cells. **j, k**, Images of the liver showing metastatic lesions (yellow, CK19) and Ki-67 (purple). Scale bars, 4 mm (**j**) and 200 μm (**k**). **l**, Quantification of lesions (left) and Ki-67^{+} tumour cells (right). Data representative of one experiment (**g–l**). **m**, Images of SAA detected by immunohistochemistry (brown, $n = 5$ for wild-type mice orthotopically injected with PBS or PDAC cells). Dashed lines and asterisks indicate sinusoids and hepatocytes, respectively. **n**, Images of *Saa1* and *Saa2* mRNA (brown) detected by RNA in situ hybridization. Data representative of one experiment (**m, n**). Scale bars, 50 μm unless indicated otherwise. Statistical significance calculated using one-way ANOVA with Dunnett's test. NS, not significant. Data represented as mean ± s.d.
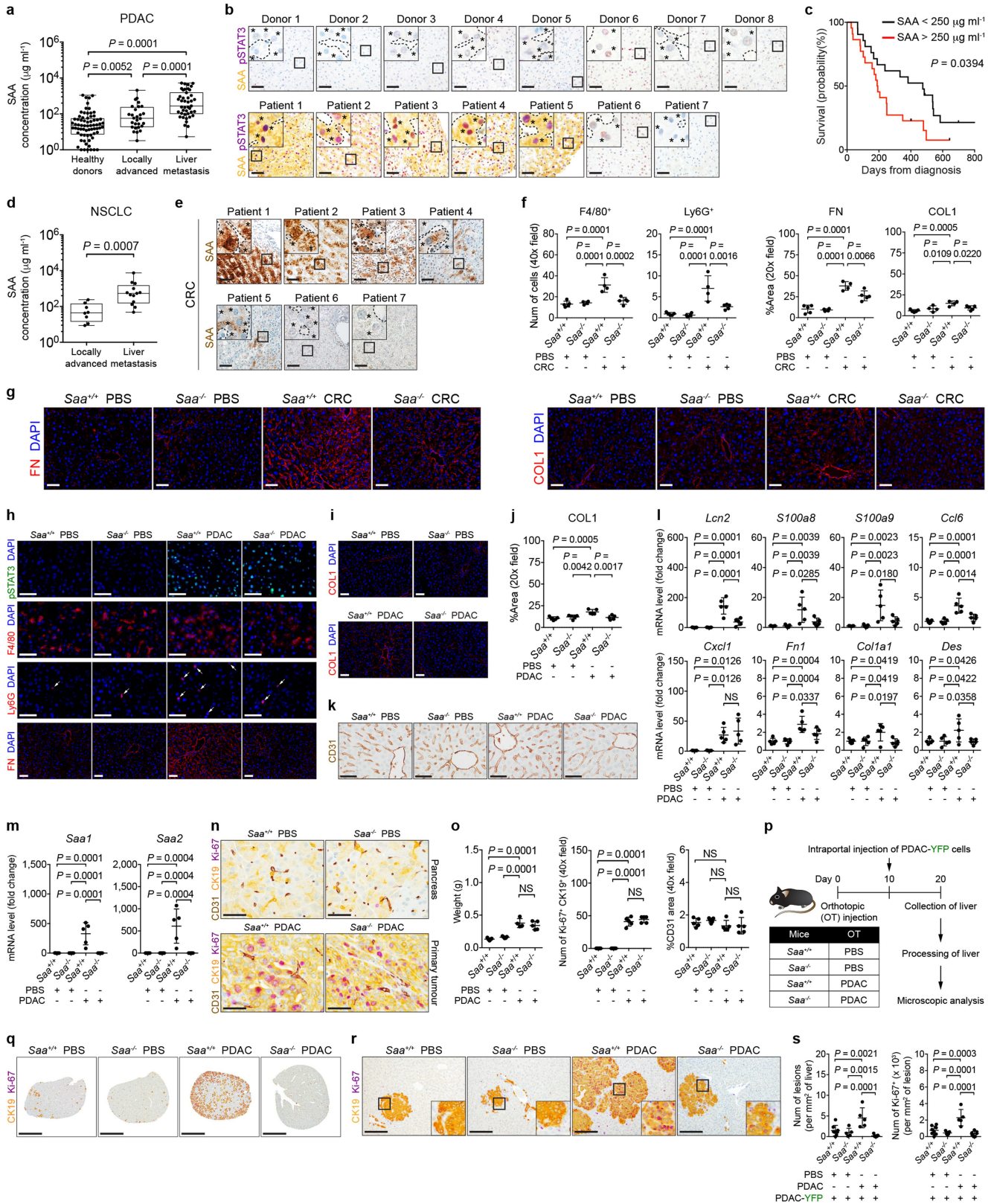
Extended Data Fig. 7 | See next page for caption.

Extended Data Fig. 7 | SAA promotes the formation of a pro-metastatic niche in the liver. a, Concentration of circulating SAA in healthy donors ($n = 69$), patients with locally advanced PDAC ($n = 28$), and patients with liver metastases ($n = 43$). Data represented as a box plot (centre line, median; box limits, upper and lower quartiles; whiskers, max and min values). **b**, Images of SAA (yellow) and pSTAT3 (purple) in the liver of healthy donors and patients with PDAC with liver metastases. Dashed lines and asterisks indicate sinusoids and hepatocytes, respectively. **c**, Kaplan–Meier survival curve for patients with PDAC with liver metastases who had low ($<250\,\mu g\,ml^{-1}$, black, $n = 21$) or high ($>250\,\mu g\,ml^{-1}$, red, $n = 22$) levels of circulating SAA. **d**, Concentration of circulating SAA in patients with locally advanced NSCLC ($n = 8$) and patients with NSCLC with liver metastases ($n = 13$). Data shown as a box plot (centre line, median; box limits, upper and lower quartiles; whiskers, max and min values). **e**, Images of SAA (brown) in the liver of CRC patients with liver metastases. Dashed lines and asterisks indicate sinusoids and hepatocytes, respectively. Data representative of one experiment (**a**–**e**). **f**, **g**, $n = 5$ and 4 for $Saa^{+/+}$ mice and $n = 4$ and 5 for $Saa^{-/-}$ mice orthotopically injected with PBS or CRC cells (MC-38), respectively. **f**, Quantification of myeloid cells, fibronectin, and COL1. **g**, Images of fibronectin (left) and COL1 (right). Data representative of one experiment (**f**, **g**). **h**–**o**, $n = 5$ for all

groups unless indicated otherwise. **h**, Images of pSTAT3+ cells, myeloid cells, and fibronectin. **i**, **j**, Images and quantification of COL1. **k**, Images of sinusoids (brown, CD31) in the liver. **l**, mRNA levels of *Lcn2*, *S100a8*, *S100a9*, *Ccl6*, *Cxcl1*, *Fn1*, *Col1a1*, and *Des* in the liver. **m**, mRNA levels of *Saa1* and *Saa2*. **n**, Images of pancreas and primary tumour stained for CD31 (brown), CK19 (yellow), and Ki-67 (purple). **o**, Quantification of the weight of pancreas or primary tumour (left), number of Ki-67+ tumour cells (middle), and vascular area (right). For weight, $n = 4$ for $Saa^{+/+}$ mice injected with PDAC cells. Data representative of one (**i**–**k**, *Fn1*, *Col1a1*, and *Des* in **l**, **n**, **o**) or two independent experiments (**h**, all other genes in **l**, **m**). **p**, Study design for **q**–**s** ($n = 8$ and 5 for $Saa^{+/+}$ mice and $n = 5$ and 7 for $Saa^{-/-}$ mice injected with PBS and PDAC cells, respectively). All groups were injected with PDAC–YFP cells on day 10. **q**, **r**, Images of the liver showing metastatic lesions (yellow, CK19) and Ki-67 (purple). Scale bars, 4 mm (**q**) and 200 μm (**r**). **s**, Quantification of lesions (left) and Ki-67+ tumour cells (right). Data representative of one experiment (**p**–**s**). Scale bars, 50 μm unless indicated otherwise. Statistical significance calculated using two-sided Mann–Whitey test (**a**, **d**), Mantel–Cox test (**c**), and one-way ANOVA with Dunnett's test (other panels). NS, not significant. Data represented as mean ± s.d. unless indicated otherwise.
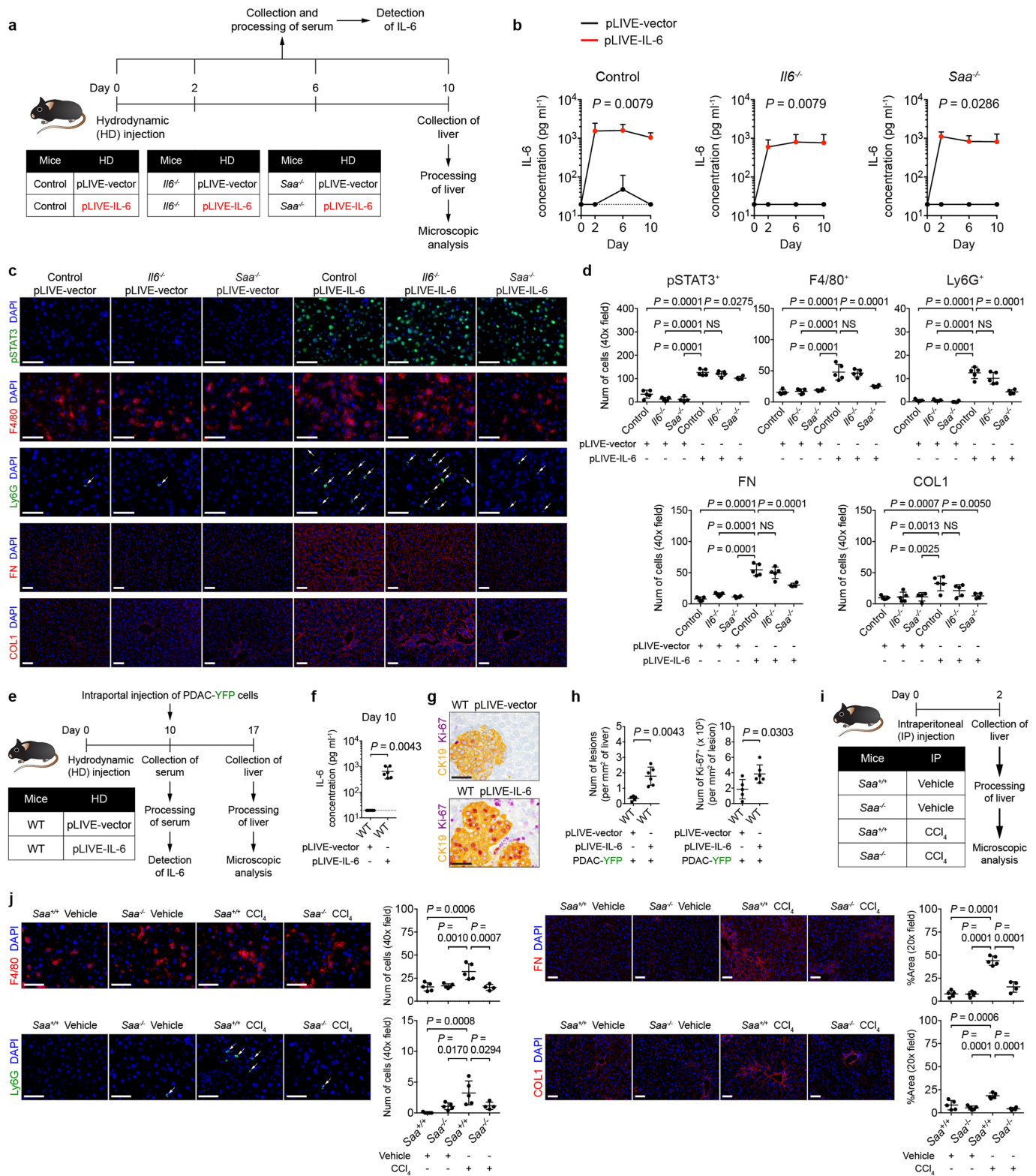
Extended Data Fig. 8 | SAA is a downstream mediator of IL-6 signalling that drives myeloid cell accumulation and fibrosis within the liver.
**a**, Study design for **b–d** ($n = 5$ for all groups, except $n = 4$ for $Saa^{-/-}$ mice). **b**, Concentration of IL-6 in the serum collected from control mice (left), $Il6^{-/-}$ mice (middle), and $Saa^{-/-}$ mice (right) on indicated days. **c**, **d**, Images and quantification of pSTAT3^{+} cells, myeloid cells, fibronectin, and COL1. Arrows indicate Ly6G^{+} cells. Data representative of one experiment (**a–d**). **e**, Study design for **f–h** ($n = 5$ for mice injected with pLIVE-vector; $n = 6$ for mice injected with pLIVE-IL-6). **f**, Concentration of IL-6 in the serum. **g**, Images of the liver showing

metastatic lesions (yellow, CK19) and Ki-67 (purple). **h**, Quantification of lesions (left) and Ki-67^{+} tumour cells (right). Data representative of one experiment (**e–h**). **i**, Study design for **j** ($n = 5$ for all groups, except $n = 4$ for $Saa^{-/-}$ mice injected with CCl$_4$). **j**, Images and quantification of myeloid cells, fibronectin, and COL1. Arrows indicate Ly6G^{+} cells. Data representative of one experiment (**i**, **j**). Dashed lines indicate the lower limit of detection (**b**, **f**). Scale bars, 50 μm. Statistical significance calculated using two-tailed Mann–Whitney test (**b**, **f**, **h**) or one-way ANOVA with Dunnett's test (other panels). NS, not significant. Data represented as mean + s.d. or mean ± s.d.
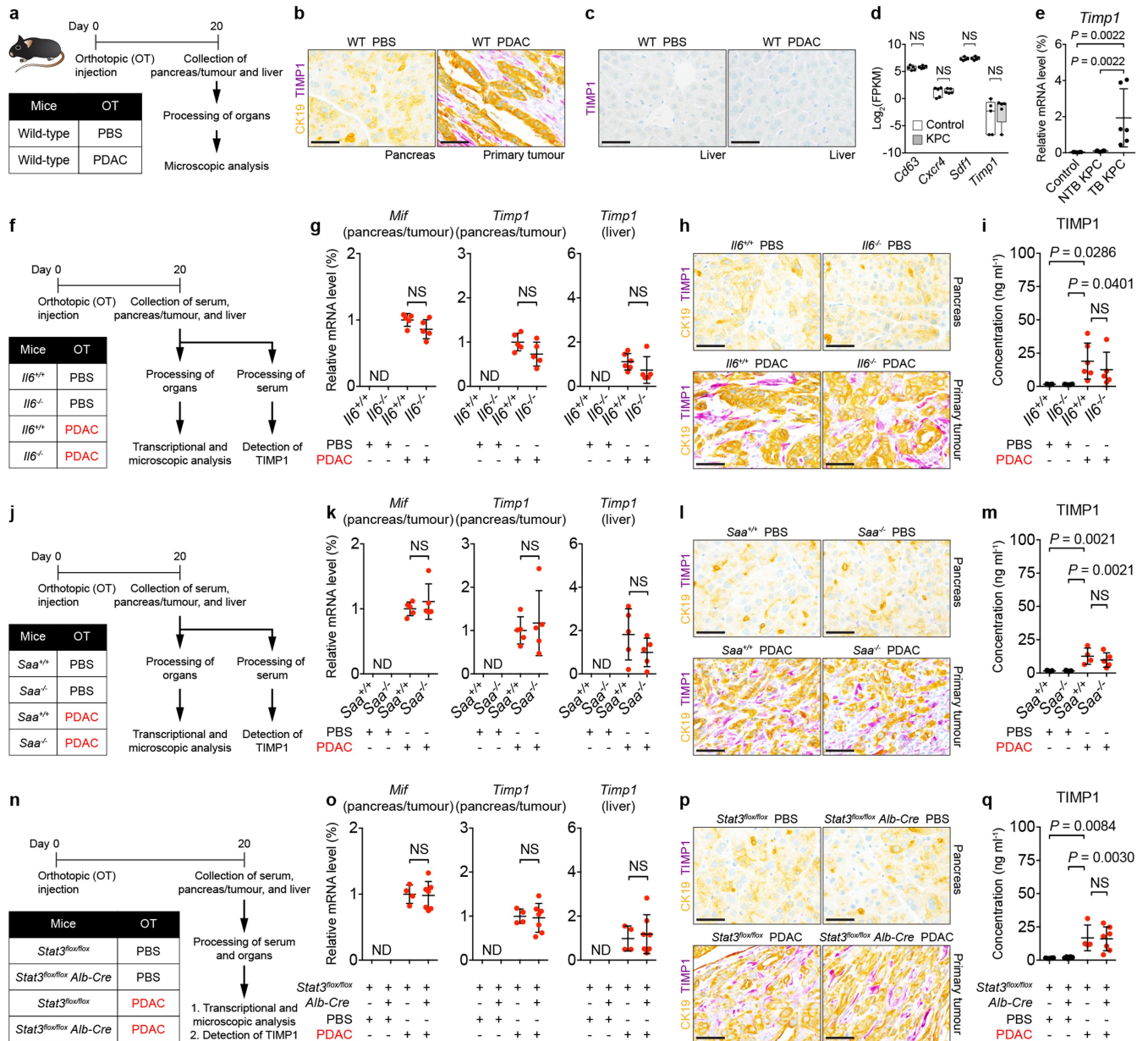
Extended Data Fig. 9 | IL-6–STAT3–SAA signalling axis does not affect expression of MIF and TIMP1. a, Study design for **b–e** (*n* = 5 and 4 for mice injected with PBS and PDAC cells). **b, c**, Images of CK19 (yellow) and TIMP1 (purple) in the pancreas, primary tumour, and liver. Data representative of at least three independent experiments (**a–c**). **d**, FPKM values of genes in the liver of control mice (*n* = 5) and NTB KPC mice (*n* = 5) obtained from QuantSeq 3′ mRNA sequencing. Data represented as box plots (centre line, median; box limits, upper and lower quartiles; whiskers, max and min values). **e**, mRNA levels of *Timp1* in the liver of control mice (*n* = 6), NTB KPC mice (*n* = 7), and tumour-bearing KPC mice (*n* = 6) relative to *Actb*. Data representative of one experiment (**d, e**). **f, j, n**, Study designs for **g–i, k–m** and **o–q**, respectively. For **f**, *n* = 5 for *Il6*$^{+/+}$ mice injected with PBS and *n* = 5 or 6 for *Il6*$^{+/+}$ mice injected with

PDAC cells. *n* = 4 and 5 for *Il6*$^{−/−}$ mice injected with PBS and PDAC cells, respectively. For **j**, *n* = 5 for all groups, except *n* = 4 or 5 for *Saa*$^{+/+}$ injected with PDAC cells. For **n**, *n* = 4 for *Stat3*$^{flox/flox}$ mice and *n* = 8 and 7 for *Stat3*$^{flox/flox}$ *Alb-cre* mice injected with PBS and PDAC cells, respectively. **g, k, o**, mRNA levels of *Mif* and *Timp1* in the indicated organs relative to *Actb*. **h, l, p**, Images of CK19 (yellow) and TIMP1 (purple) in the pancreas and primary tumour. **i, m, q**, Concentration of TIMP1 in the serum. Data representative of one experiment (**f–q**). Scale bars, 50 μm. Statistical significance calculated using one-way ANOVA with Dunnett's test (**i, m, q**) or two-tailed Mann–Whitney test (other panels). NS, not significant. ND, not detected. Data represented as mean ± s.d. unless indicated otherwise.
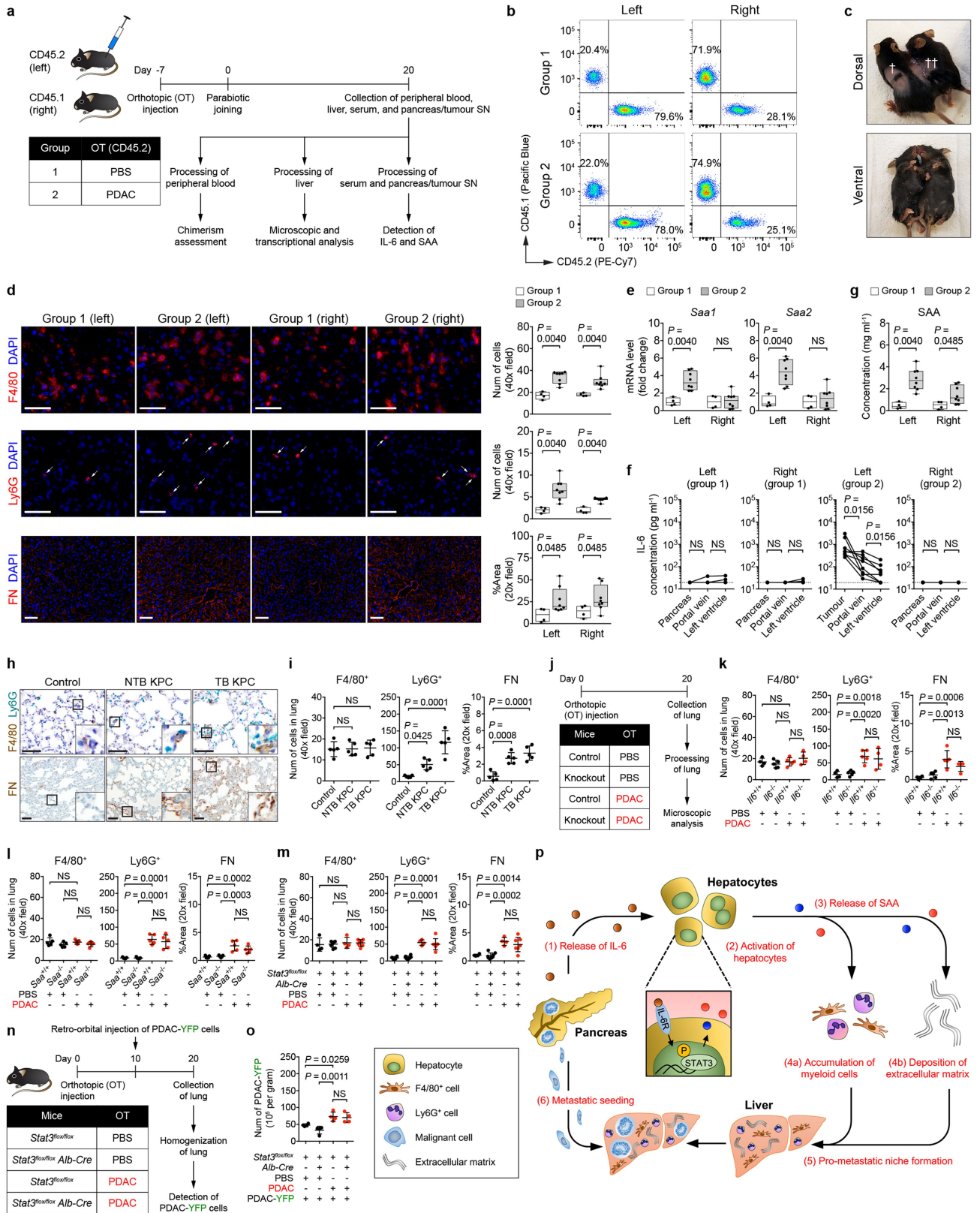
Extended Data Fig. 10 | See next page for caption.

Extended Data Fig. 10 | Primary PDAC development induces a systemic response that promotes the formation of a pro-metastatic niche in the liver. a, Study design for **b**–**g** ($n = 4$ and 8 for CD45.2 mice injected with PBS (group 1) and PDAC cells (group 2), respectively). **b**, Assessment of chimaerism in parabiotically joined mice. Flow cytometric analysis of peripheral blood gated on CD45.1$^+$ and CD45.2$^+$ cells as a percentage of CD45$^+$ cells. **c**, Dorsal (top) and ventral (bottom) views of parabiotically joined mice. Dagger, site of laparotomy for orthotopic injection; double dagger, skin suture for parabiotic joining. **d**, Images and quantification of myeloid cells and fibronectin. Arrows indicate Ly6G$^+$ cells. **e**, mRNA levels of *Saa*. **f**, Concentration of IL-6 in pancreas supernatant and serum. Solid lines indicate data points from individual mice. Dashed lines indicate the lower limit of detection. **g**, Concentration of circulating SAA. Data representative of one (**f**, **g**) or two independent experiments (**a**–**e**). **h**, **i**, $n = 5$ for all groups. **h**, Images of myeloid cells and fibronectin in the lung of control mice, NTB KPC mice, and tumour-bearing KPC mice. **i**, Quantification of myeloid cells and fibronectin. Data representative of

one experiment (**h**, **i**). **j**, Study design for **k**–**m**. **k**, $n = 4$ and 5 for *Il6*$^{+/+}$ mice and $n = 5$ and 4 for *Il6*$^{-/-}$ mice injected with PBS and PDAC cells, respectively. For **l**, $n = 5$ for all groups. For **m**, $n = 4$ for *Stat3*$^{flox/flox}$ mice and $n = 8$ and 7 for *Stat3*$^{flox/flox}$ *Alb-cre* mice injected with PBS and PDAC cells, respectively. **k**–**m**, Quantification of myeloid cells and fibronectin. Data representative of one experiment (**j**–**m**). **n**, Study design for **o** ($n = 4$ for all groups of mice). All groups of mice were injected with PDAC–YFP cells on day 10. **o**, Quantification of PDAC–YFP cells. Data representative of one experiment (**n**, **o**). **p**, Conceptual model of generation of pro-metastatic niche in the liver. Scale bars, 50 μm. Statistical significance calculated using two-sided Mann–Whitney test (**d**, **e**, **g**), two-sided Wilcoxon test (**f**), and one-way ANOVA with Dunnett's test (other panels). NS, not significant. Data represented as mean ± s.d., except **d**, **e**, **g**, which are shown as box plots (centre line, median; box limits, upper and lower quartiles; whiskers, max and min values). Data from individual mice are shown in **f**.

nature research

Corresponding author(s):	Gregory L. Beatty
Last updated by author(s):	Feb 22, 2019

Reporting Summary

Nature Research wishes to improve the reproducibility of the work that we publish. This form provides structure for consistency and transparency in reporting. For further information on Nature Research policies, see Authors & Referees and the Editorial Policy Checklist.

Statistics

For all statistical analyses, confirm that the following items are present in the figure legend, table legend, main text, or Methods section.

n/a	Confirmed	
☐	☒	The exact sample size (n) for each experimental group/condition, given as a discrete number and unit of measurement
☐	☒	A statement on whether measurements were taken from distinct samples or whether the same sample was measured repeatedly
☐	☒	The statistical test(s) used AND whether they are one- or two-sided *Only common tests should be described solely by name; describe more complex techniques in the Methods section.*
☐	☒	A description of all covariates tested
☐	☒	A description of any assumptions or corrections, such as tests of normality and adjustment for multiple comparisons
☐	☒	A full description of the statistical parameters including central tendency (e.g. means) or other basic estimates (e.g. regression coefficient) AND variation (e.g. standard deviation) or associated estimates of uncertainty (e.g. confidence intervals)
☐	☒	For null hypothesis testing, the test statistic (e.g. F, t, r) with confidence intervals, effect sizes, degrees of freedom and P value noted *Give P values as exact values whenever suitable.*
☒	☐	For Bayesian analysis, information on the choice of priors and Markov chain Monte Carlo settings
☒	☐	For hierarchical and complex designs, identification of the appropriate level for tests and full reporting of outcomes
☒	☐	Estimates of effect sizes (e.g. Cohen's d, Pearson's r), indicating how they were calculated

Our web collection on statistics for biologists contains articles on many of the points above.

Software and code

Policy information about availability of computer code

Data collection	Flow cytometric data and cytometric bead array data were collected using FACSDiva (BD Biosciences, version 8.0.1).
Data analysis	Flow cytometric data were analysed using FlowJo (FlowJo, version 10.2). Cytometric bead array data were analysed using FCAP Array (BD Biosciences, version 3.0). QuantSeq 3' mRNA sequencing data were aligned using RNA-Seq Alignment application (version 1.0.0) and analysed using Cufflinks Assembly & DE application (version 2.1.0) in the BaseSpace Suite (Illumina). Differentially expressed genes were analysed using ClueGO (version 2.3.3, Ref 35) and CluePedia (version 1.3.3, Ref 36), which are applications of Cytoscape software (version 3.5.1, Ref 37). Gene set enrichment analysis (GSEA, version 3.0, Ref 40) was used to determine biological processes that were differentially enriched in experimental groups. Statistical significance was calculated using Prism (GraphPad Software, version 7).

For manuscripts utilizing custom algorithms or software that are central to the research but not yet described in published literature, software must be made available to editors/reviewers. We strongly encourage code deposition in a community repository (e.g. GitHub). See the Nature Research guidelines for submitting code & software for further information.

Data

Policy information about availability of data

All manuscripts must include a data availability statement. This statement should provide the following information, where applicable:

- Accession codes, unique identifiers, or web links for publicly available datasets
- A list of figures that have associated raw data
- A description of any restrictions on data availability

QuantSeq 3' mRNA sequencing data have been deposited in the Gene Expression Omnibus (GEO) under accession number GSE109480. Source data are provided for all figures and extended data figures. All data are available from the corresponding author upon reasonable request.

Field-specific reporting

Please select the one below that is the best fit for your research. If you are not sure, read the appropriate sections before making your selection.

☒ Life sciences   ☐ Behavioural & social sciences   ☐ Ecological, evolutionary & environmental sciences

For a reference copy of the document with all sections, see nature.com/documents/nr-reporting-summary-flat.pdf

Life sciences study design

All studies must disclose on these points even when the disclosure is negative.

Sample size	Sample sizes were estimated based on pilot experiments conducted in our laboratory and were selected to provide sufficient numbers of mice in each group to yield a two-sided statistical test, with the potential to reject the null hypothesis with a power (1 - beta) of 80%, subject to alpha = 0.05.
Data exclusions	Mice that were euthanized early due to health concerns or surgical complications were excluded from studies as pre-established by the University of Pennsylvania IACUC protocol #803605.
Replication	Unless indicated otherwise in the figure legends, experimental findings were reliably reproduced in at least two independent experiments. Co-housed littermates were used for animal studies.
Randomization	Mice of similar age and gender were block randomized to experimental groups.
Blinding	Investigators were not blinded to most studies as interventions required knowledge of the individual experimental groups. To establish objective measurements from studies incorporating immunohistochemistry and immunofluorescence microscopy, 5 random fields were collected per replicate, and cell counts in each field were averaged for every biological replicate.

Reporting for specific materials, systems and methods

We require information from authors about some types of materials, experimental systems and methods used in many studies. Here, indicate whether each material, system or method listed is relevant to your study. If you are not sure if a list item applies to your research, read the appropriate section before selecting a response.

Materials & experimental systems

n/a	Involved in the study
☐	☒ Antibodies
☐	☒ Eukaryotic cell lines
☒	☐ Palaeontology
☐	☒ Animals and other organisms
☐	☒ Human research participants
☒	☐ Clinical data

Methods

n/a	Involved in the study
☒	☐ ChIP-seq
☐	☒ Flow cytometry
☒	☐ MRI-based neuroimaging

Antibodies

Antibodies used	In vivo and ex vivo studies: Antibodies to CD4 (clone GK1.5, 0.2 mg/injection, cat#BE0003-1), CD8 (clone 2.43, 0.2 mg/injection, cat#BE0061), IL-6R (clone 15A7, 0.2 mg/injection, cat#BE0047), and isotype control (clone LTF-2, 0.2 mg/injection, cat#BE0090) were purchased from BioXCell (NH, USA). Flow cytometry: Mouse-specific antibodies used in all flow cytometric phenotyping included CD3 (clone 17A2, dilution 1:100, BioLegend, cat#100214), CD4 (clone RM4-5, dilution 1:100, eBioscience, cat#17-0042-82), CD4 (clone RM4-5, dilution 1:100, BioLegend, cat#100510), CD8 (clone 53-6.7, dilution 1:100, BioLegend, cat#100722), CD8 (clone YTS156.7.7, dilution 1:100, BioLegend, cat#126607), CD11b (clone M1/70, dilution 1:100, BD Biosciences, cat#550993), CD19 (clone 1D3/CD19, dilution 1:100, BioLegend, cat#152410), CD44 (clone IM7, dilution 1:100, eBioscience, cat#12-0441-82), CD45 (clone 30-F11, dilution 1:800, BD Biosciences, cat#552848), CD45.1 (clone A20, dilution 1:100, BioLegend, cat#110722), CD45.2 (clone 104, dilution 1:100, BioLegend, cat#109830), CD62L (clone MEL-14, dilution 1:100, Thermo Fisher, cat#A15409), F4/80 (clone BM8, dilution 1:100, eBioscience, cat#11-4801-85), and Ly6G (clone 1A8, dilution 1:800, BD Biosciences, cat#56062). Manual immunohistochemistry and immunofluorescence: Antibodies to albumin (polyclonal, dilution 1:100, cat#ab106582), FN (polyclonal, dilution 1:200, cat#ab2413), and COL1 (polyclonal, dilution 1:200, cat#ab34710) were purchased from Abcam (MA, USA). Antibody to Ly6G (clone 1A8, dilution 1:100, cat#BE0075-1) was purchased from BioXCell (NH, USA). Antibody to pSTAT3 (clone D3A8, dilution 1:50, cat#9145S) was purchased from Cell Signaling (MA, USA). Antibody to amyloid A (polyclonal, dilution 1:2000) was obtained from de Beer Lab*.

Antibody to F4/80 (clone BM8, dilution 1:80, cat#14-4801) was purchased from eBioscience (MA, USA). *Reference: Webb, N. R. et al. Arterioscler. Thromb. Vasc. Biol. 35, 1156–1165 (2015).

Automated immunohistochemistry and immunofluorescence:
Antibodies to alpha-SMA (polyclonal, dilution 1:100, cat#ab5694), CD4 (clone EPR19514, dilution 1:100, cat#ab183685), CD8 (clone EPR20305, dilution 1:100, cat#ab209775), CK19 (clone EPNCIR127B, dilution 1:800, cat#ab133496), F4/80 (clone CI:A3-1, dilution 1:100, cat#ab6640), FN (clone EPR19241-46, dilution 1:100, cat#ab199056), pSTAT3 (clone E121-31, clone 1:100, cat#ab32143), and TIMP1 (clone RM0136-6A34, dilution 1:100, cat#ab86482) were purchased from Abcam (MA, USA). Antibody to Ly6G (clone 1A8, dilution 1:100, cat#BE0075-1) was purchased from BioXCell (NH, USA). Antibodies to CD31 (clone D8V9E, dilution 1:50, cat#77699) and Ki-67 (clone D3B5, dilution 1:200, cat#12202) were purchased from Cell Signaling (MA, USA). Antibody to amyloid A (clone MC1, dilution 1:50, cat#M075901-2) was purchased from Dako (CA, USA). Antibodies to CD31 (clone JC70, no dilution, cat#760-4378) and CK19 (clone A53-B/A2.26, no dilution, cat#760-4281) were purchased from Ventana (CA, USA).

| Validation | Antibodies were validated according to the manufacturer's instructions. Mouse splenocytes and human and mouse tissue specimens (e.g., liver and pancreatic tumour) were to validate antibodies. More details for antibodies used in our studies can be found in Supplementary Table 3. |

Eukaryotic cell lines

Policy information about cell lines

Cell line source(s)	PDA.69 and PDA.8572 are cell lines that were derived from primary pancreatic tumours as previously described (Ref 26). These tumours arose spontaneously in KPC mice that had been backcrossed onto the C57BL/6 background for >10 generations. MC-38 cell line was purchased from Kerafast.
Authentication	Cell line authentication was based on histological analysis of the implanted cell line with comparison to the primary tumour from which the cell line was derived.
Mycoplasma contamination	Cell lines were tested routinely for Mycoplasma contamination using MycoAlert (Cambrex) at the Cell Center Services Facility at the University of Pennsylvania. All cell lines used in our studies tested negative for Mycoplasma contamination.
Commonly misidentified lines (See ICLAC register)	No commonly misidentified cell lines were used.

Animals and other organisms

Policy information about studies involving animals; ARRIVE guidelines recommended for reporting animal research

Laboratory animals	CD45.2 (wild-type, C57BL/6J), CD45.1 (B6.SJL-Ptprca Pepcb/BoyJ), Il-6 knockout (Il6-/-, B6.129S2-Il6tm1Kopf/J), Stat3flox/flox (B6.129S1-Stat3tm1Xyfu/J), and Albumin-Cre+/+ (B6.Cg-Tg(Alb-cre)21Mgn/J) mice were obtained from the Jackson Laboratory. Stat3flox/flox mice and Albumin-Cre+/+ mice were bred to each other to generate Stat3flox/flox Albumin-Cre mice as described in the Materials and Methods under "Animals." KPC mice and PC mice were previously described (Ref 4 and 5). Saa-/- mice were provided by the University of Kentucky College of Medicine and were previously described (Ref 31). Male and female mice aged between 8-12 weeks were used unless indicated otherwise. Mice were age- and gender-matched with appropriate control mice for analysis.
Wild animals	Our study did not involve wild animals.
Field-collected samples	The study did not involve samples collected from the field.
Ethics oversight	Animal protocols were reviewed and approved by the Institute of Animal Care and Use Committee of the University of Pennsylvania.

Note that full information on the approval of the study protocol must also be provided in the manuscript.

Human research participants

Policy information about studies involving human research participants

| Population characteristics | Plasma samples from healthy donors (age 37-80, 33 males and 36 females), PDAC patients with locally advanced disease (age 50-88, 18 males and 10 females), PDAC patients with liver metastases (age 38-85, 26 males and 17 females), NSCLC patients with locally advanced disease (age 63-86, 5 males and 3 females), and NSCLC patients with liver metastases (age 40-79, 6 males and 7 females) were used.

Liver biopsies from healthy donors (age 24-39, 4 males and 4 females), PDAC patients with liver metastases (age 57-85, 5 males and 2 females), and CRC patients (7 samples in total, limited information on age and gender) were used.

Detailed characteristics of healthy donors and patients are shown in Supplementary Table 2. |
| Recruitment | Patients at the University of Pennsylvania Health System (Penn Medicine) and the Mayo Clinic were recruited for our studies. All patient samples were obtained after written consent and were de-identified. There was no self-selection bias. |

Ethics oversight	Studies were conducted in accordance with the 1996 Declaration of Helsinki and approved by the institutional review boards of the University of Pennsylvania and the Mayo Clinic.

Note that full information on the approval of the study protocol must also be provided in the manuscript.

Flow Cytometry

Plots

Confirm that:

☒ The axis labels state the marker and fluorochrome used (e.g. CD4-FITC).

☒ The axis scales are clearly visible. Include numbers along axes only for bottom left plot of group (a 'group' is an analysis of identical markers).

☒ All plots are contour plots with outliers or pseudocolor plots.

☒ A numerical value for number of cells or percentage (with statistics) is provided.

Methodology

Sample preparation	Mice were euthanized, and the liver and lung were harvested after draining the blood by severing the portal vein and inferior vena cava. The liver and lung were rinsed thoroughly in PBS before mincing with micro dissecting scissors into small pieces (< 0.5 0.5 mm in size) at 4 C in DMEM containing collagenase (1 mg/ml, Sigma-Aldrich), DNase (150 U/ml, Roche), and Dispase (1 U/ml, Worthington). Tissues were then incubated at 37 C for 30 minutes with intermittent agitation, filtered through a 70-um nylon strainer (Corning), and washed three times with DMEM. Cells were resuspended in ACK lysing buffer (Life Technologies) at room temperature for 15 minutes to remove red blood cells. After washing three times with DMEM, cells were counted and stained using Aqua dead cell stain kit (Life Technologies) following manufacturer's protocol. For characterization of immune cell subsets, cells were washed three times with PBS containing 0.2 mM EDTA with 2% FBS and stained with appropriate antibodies (Supplementary Table 3). For quantification of PDAC-YFP cells, cells were not stained with any antibodies. Lastly, cells were washed three times with PBS containing 0.2 mM EDTA with 2% FBS. Collection and analysis of the peripheral blood was previously described (Ref 26).
Instrument	FACS Canto II (BD Biosciences).
Software	FlowJo (FlowJo, LLC, version 10.2)
Cell population abundance	Our study did not involve flow sorting.
Gating strategy	Immune cells: Total cells were gated on FSC-A vs. SSC-A, FSC-H vs. FSC-A, SSC-H vs. SSC-A, and then live/dead vs. SSC-A to identify live cells. Cells were then gated on CD45 vs. SSC-A, CD3 vs. CD19, Ly6G vs. CD11b, and F4/80 vs. CD11b to identify F4/80+, Ly6G +, CD3+, and CD19+ cells (Extended Data Fig. 1a) or CD45 vs. CD3, CD4 vs. CD8, and CD62L vs. CD44 to identify T cell subsets (Extended Data Fig. 2n). PDAC-YFP cells: Total cells were gated using the same strategy as described above to identify live cells (Extended Data Fig. 1a). Cells were then gated on YFP vs. SSC-A to determine the percentage of live cells that were YFP+.

☒ Tick this box to confirm that a figure exemplifying the gating strategy is provided in the Supplementary Information.